國立臺灣大學理學院物理學系

博士論文

Department of Physics

College of Science

National Taiwan University

Doctoral Dissertation

探索粒子天文物理學與宇宙學中的兩個面向：一. 簇射大氣螢光的實驗室量測 二. 暗能本質的現象學規範

Aspects of Particle Astrophysics and Cosmology:
I. Laboratory Measurement of Air Fluorescence from Showers
II. Constraining the Nature of Dark Energy

陳建文

Chien-Wen Chen

指導教授：黃偉彥 博士　陳丕燊 博士

Advisors: W-Y. Pauchy Hwang, Ph.D.　Pisin Chen, Ph.D.

中華民國 98 年 6 月

June, 2009

Acknowledgment

I have learned from many sincere and capable scientists during my graduate school years. I have my best gratitude to W-Y. Pauchy Hwang and Pisin Chen for their long time guidance and support. I am also particularly grateful for the guidance from Clive Field, Johnny Ng, Kevin Reil, and Je-An Gu. Last but not least, I thank my family and my friends for their loving support.

This thesis has been examined and approved by the committee consisting of Prof. Hsiang-Kuang Chang, Prof. Pisin Chen, Prof. Tzihong Chiueh, Prof. Li-Zhi Fang, Prof. W-Y. Pauchy Hwang, Prof. Guey-Lin Lin, Prof. Wen-Long Lin and Prof. Kin-Wang Ng. I have my sincere appreciation to the committee members for their serious examinations.

Preface

Particle astrophysics is the study of elementary particles from astronomical origin, and their relation to astrophysics and cosmology. One of its aspects is the study of cosmic rays. Cosmic rays were first discovered by V. F. Hess in 1912 [1]. He found an increase of ionizing radiations with increasing height during balloon flights up to altitudes of 5 km, and concluded that there were radiations coming into the atmosphere from outer space. Ever since the discovery, cosmic rays' compositions and sources, acceleration and propagation mechanisms, have been subjects of research. Perhaps the most puzzling questions of cosmic rays are related to those with their "ultra high" energy being measured. Particles carrying a few 10^{20} GeV energy and hitting the earth atmosphere have been observed (see Ref. [2] for the first discovery). The existence of such high energy particles can not be explained by conventional mechanisms and might be a link to new physics. Their propagation is also of great interest because of their energy loss from interacting with the cosmic microwave background photons. Thus far, no corresponding astronomical origins have been identified. The energy spectrum in this region is hard to be measured and has been obtained differently by separate observation groups.

The study of the universe has become a precision science and has developed prosperously due to the late twentieth century advances. Cosmology is the study of the large scale structures and dynamics of the universe and is concerned with fundamental questions about its formation and evolution. The now broadly accepted Big Bang theory describes that the universe was originated from a size of only a few millimeters about 14 billion years ago. The first clue that the Big Bang theory might be right was provide by E. Hubble's 1929 observation that galaxies were generally receding from earth [3].

The theory has been later supported by various observations including the discovery of the cosmic microwave background radiation [4] as the remnant heat from the Big Bang. Since Hubble's discovery, cosmologists had been trying to measure the slowing of the cosmic expansion due to gravity. However, in 1998, two teams independently found that the light from distance Type Ia supernovae were dimmer than that was expected in a decelerating universe and the expansion of the universe is speeding up [5, 6]. This cosmic acceleration is now perhaps one of the greatest puzzles in physics. Indications are that there exists an exotic energy source, termed dark energy, with sufficient negative pressure to cause this acceleration, or that Einstein's gravity theory should be modified. Ever since the discovery, intense studies have been carried out and proceeding. Various observations from ground and space have been made and proposed. Many models have been proposed, but yet none of them has been verified and each of them has its unresolved theoretical problems.

In this thesis, we investigate two aspects of particle astrophysics and cosmology, including the ultra high energy cosmic ray (UHECR) spectrum and the nature of dark energy. The first part is the FLASH experiment carried out at the SLAC National Accelerator Laboratory (SLAC). In this experiment, we study calibration factors for UHECR detectors using the air fluorescence technique. The FLASH collaboration, under the leadership of the co-spokespersons Pierre Sokolsky and Pisin Chen, includes members from SLAC, University of Montana, University of Utah, Rutgers University and Taida CosPa Center. The results have been published in Astropart. Phys. and Nucl. Instrum. Meth. A [7, 8, 9, 10]. The overall setups and results of this experiment are described in this thesis. The credit of this experiment belongs to the whole collaboration. In the second part of the thesis, we test dark energy models using a new approach and discriminate models on the phase plane of the dark energy equation of state. The results have been published in New J. Phys., Mod. Phys. Lett. A [11, 12] and submitted to Phys. Lett. B [13]. This work is done in collaboration with Je-An Gu and Pisin Chen.

中文摘要

我們探索粒子天文物理學與宇宙學中兩個最撩人興趣的問題。他們分別是超高能宇宙射線的能譜以及暗能的本質。

一. 使用地面陣列或大氣螢光觀測器是測定超高能宇宙射線能量最普遍的兩種方式。由地面陣列 AGASA 與大氣螢光觀測器 HiRes 兩者所得到的超高能宇宙射線能譜呈現明顯的差異。 FLASH 是一個致力於減少大氣螢光觀測器的能量觀測系統誤差的實驗。 我們量測被 28.5 GeV 電子束激發的空氣螢光之產率與光譜。 在一大氣壓 304 K 的乾燥空氣中，我們量測到的螢光產率是每 MeV 20.8 ± 1.6 個光子。我們也量測空氣螢光產率與 28.5 GeV 電子脈衝所引發的電磁簇射的深度的函數關係。結果證實了在量測超高能宇宙射線中使用大氣螢光量變曲線的正當性。

二. 我們對五種暗能模型做一致性測試。模型包括宇宙常數，廣義化的 Chaplygin gas，以及三種第五元素模型：指數位能，冪律位能，以及反指數位能。對於每一個模型，我們認定一個一般而言會隨紅移變化但在這模型的範疇中是常數的特徵量 Q(z)。我們進一步定義「一致性度量」M(z)為 Q(z)對紅移的導數。如果一個模形與觀測相符，觀測應該允許對應的 M(z)的值為零。採用了一個被廣泛使用的暗能狀態方程式參數化並且使用目前 SNIa，CMB，以及 BAO 的觀測資料後，我們發現指數位能模型在 95.4%的信心程度下被排除。這套方法的鑑別力以及由於選擇的參數化可能造成的偏見應該在未來用 Monte Carlo test 來檢驗。暗能模型在 w-w’ 平面的分類已經在文獻上被研究了。 其中 w 是暗能狀態方程式而 w’ 是它以哈伯時間為單位的時間導數。 我們使用同樣的觀測資料以及採用同樣的暗能狀態方程式參數化而得到 w-w’ 平面上的約束。 我們發現包括宇宙常數，魅影，非魅影 barotropic 流體，還有單調上滾的第五元素等暗能模型在 68.3% 的信心程度下被目前的觀測資料排除。下滾的第五元素包括解凍與凍結模型和目前的觀測相符．所有上列的模型在 95.4% 的信心程度仍然與觀測資料相符。

關鍵字： 超高能宇宙射線，大氣簇射， 大氣螢光， 暗能， 一致性測試， 暗能狀態方程式

Abstract

We investigate the most tantalizing problems in particle astrophysics and cosmology, that is, the ultra high energy cosmic ray (UHECR) spectrum and the nature of dark energy, respectively.

I. The two most common methods to determine the energy of UHECR are ground arrays and fluorescence detectors. The results from the ground array AGASA and the fluorescence detector HiRes present a significant discrepancy in the UHECR spectrum. The Fluorescence in Air from Shower (FLASH) experiment is an effort to reduce the systematic uncertainty in energy determination for fluorescence detectors. We measure the yield and spectrum of fluorescence in air, excited by a 28.5 GeV electron beam. In atmospheric pressure, dry air at 304 K, the total yield of 20.8 ± 1.6 photons per MeV is obtained. We also measure the air fluorescence as a function of depth in electromagnetic showers initiated by bunches of 28.5 GeV electrons. The light yield is compared with the expected and observed depth profiles of ionization in the showers. The results validate the use of atmospheric fluorescence profiles in measuring ultra high energy cosmic rays.

II. We perform consistency test of five dark energy models, including the cosmological constant, the generalized Chaplygin gas, and three quintessence models: exponential, power-law and inverse-exponential potentials. For each model, we identify a "Characteristic", Q(z), which in general can vary with the redshift but is equivalent to a constant parameter within the domain of the model. We further define the "Measure of Consistency", $\mathcal{M}(z)$, as the derivative of Q(z) with respect to the redshift z. The observational data should allow a null value for $\mathcal{M}(z)$ if the corresponding dark energy models is consistent with them. With the adoption of a broadly used parametrization of the dark energy equation of state, we find that the exponential potential is ruled out at the 95.4% confidence level based on the combined data set of current SN Ia, CMB, and BAO data. The issues of discriminating power of the method and possible bias imposed by the chosen parameterization should be further studied via the Monte Carlo test in the future. Classification of dark energy models in the plane of w and w', where w is the dark energy equation of state and w' its time-derivative in units of the Hubble time, has been studied in the literature. We take the same data set, invoke the same parametrization of the dark energy equation of state, and obtain the constraints on the w–w' plane. We find that dark energy models including the cosmological constant, phantom, non-phantom barotropic fluids, and monotonic up-rolling quintessence are ruled out at the 68.3% confidence level based on the current observational data. Down-rolling quintessence, including the thawing and the freezing models, is consistent with the current observations. All the above-mentioned models are still consistent with the data at the 95.4% confidence level.

Keywords: ultra high energy cosmic rays, air shower, air fluorescence, dark energy, consistency test, dark energy equation of state

Contents

List of Figures

Part I

Laboratory Measurement of Air Fluorescence from Showers

Chapter 1

Introduction

1.1 Ultra High Energy Cosmic Rays

Cosmic rays are relativistic particles from extraterrestrial sources that hit the Earth atmosphere. Their energies have been observed to range from GeV to a few 10^{20} eV, over which the flux decreases by more than 30 orders of magnitude. Almost a century after the discovery by Victor Hess in 1912, their sources, compositions and propagation mechanisms are still subject of intense research.

Recent experimental and theoretical interests are focused on the highest energy range of cosmics rays (see Ref. [14, 15] for reviews). Ultra high energy cosmic rays (UHECR) have energy above 10^{18} eV. They are of great interest since the existence of such high energy particles can not be explained by conventional mechanisms. With energy several orders of magnitude higher then that can be generated in the laboratory, they may provide the possibility for us to uncover new physics. Theocratical explanations are proposed including the acceleration by very energetic sources [16] and the decay of primordial super-heavy particle [17]. Precise measurement of the UHECR spectrum is required to examine and distinguish between mechanisms.

An interesting aspect of UHECR is their interaction with the cosmic microwave background (CMB) photons along their propagation from the sources to the earth. In 1966, Greisen, Zatsepin and Kuzmin proposed an upper limit to the cosmic ray spectrum [18]. Protons with energy above the the threshold of $\sim 6 \times 10^{19}$ eV would rapidly lose their energy due to the interactions with the CMB photons via photonpion production. This effect is usually called GZK cutoff, which should be manifested by the suppression in the UHECR flux above the threshold energy. This strong energy-loss mechanism should also limit the source distances of UHECR above the threshould energy to less than ~ 50 Mpc. The large ground array AGASA has reported an unbroken UHECR spectrum without observation of the GZK cutoff [19]. However, the atmospheric fluorescence detector HiRes has observed the GZK cutoff with a statistical significance of five standard deviations [20]. The strong suppression of the energy spectrum is confirmed by the Pierre Auger observatory, whose energy scale is also set by fluorescence measurements [21]. Although both the latter two detectors observe the suppression, they do not agree on the flux, nor the slope exponents of the spectrum. Uncertainty in the knowledge of air fluorescence from cosmic ray showers may contribute to these differences.

It is anticipated that new experiments [22], at various stages of development, will provide access to the relative contributions of the galactic and extragalactic fluxes, the anisotropy of the arrival directions and the composition of UHECR, as well as more super GZK particles (see Ref. [15] for a review). Most of these experiments include at least a fluorescence detector. More precise measurements of the spectral and absolute fluorescence yield and its dependence on atmospheric parameters are pressingly needed.

1.2 UHECR Fluorescence Detectors

Fluorescence detectors reconstruct the primary cosmic ray energy by measuring the total fluorescence light yield generated by the atmospheric shower. When the primary cosmic ray arrive the Earth atmosphere, it hits the nuclei of the air, and produce secondary particles. The first interaction takes place in the top 10% of the atmosphere. Most of the secondary particles are pions. Neutral pions quickly decay into gamma-rays. Gamma-rays generate electrons and positrons by the pair-production process. Electrons and positrons in turn produce more gamma-rays by the bremsstrahlung mechanism. The electromagnetic shower is built up in this cascade process. The dominant absorption of the primary cosmic ray energy is the dissipative process in which the molecules of the atmosphere get either ionized or excited.

The electrons and positrons of the shower transfer energy to the air molecules by ionization and excitation and cause them to emit fluorescence light. The energy transfer is well described by the Bethe-Bloch equation [23]. Below the critical energy, ~ 86 MeV in air, the energy loss of an electron from ionization overcomes that from particle production. Therefore, a large fraction of the energy transfer comes from particles in the energy range of tens of MeV. The energy flow within the air molecules is complicated because of the number of energy levels available, and the competition between fluorescent emission and the collisional de-excitation of the air molecules, which is pressure and temperature dependent. Yet the theoretical modeling and calculation of the fluorescent light yield is being studied and progressing [24, 25, 26, 27].

The fluorescence light is emitted isotropically from the atmospheric shower. The UHECR fluorescence detectors use spherical mirrors to focus the fluorescence light on arrays of photomultiplier tubes (see Ref. [20] for example). The shower trajectory is reconstructed based on the arrival timings and angles of the light. Air fluorescence light is useful for cosmic ray measurements because its wavelength range is between 300 and 400 nm, where the atmosphere exhibits almost no absorption and there is low background light. In this wavelength range the fluorescence light is dominated by nitrogen emission lines, with major bands containing $\sim 95\%$ of light near 315, 337, 357, 380 and 391 nm [24, 28]. Modern fluorescence detectors can capture very high energy events at distances exceeding 30 km. At such distances the λ^{-4} wavelength dependence of Rayleigh scattering by atmospheric molecules becomes important. It preferentially reduces the detection efficiency of the shorter wavelengths. At 337 nm, for example, the exponential scattering length at one atmosphere is 11 km. The corrections for this require a detailed knowledge of the spectrum of the fluorescence light.

In fact, the uncertainty on the fluorescence yield remains the largest single contribution to the overall uncertainty in UHECR energy measurements using the fluorescence technique. The fluorescence yield is being studied experimentally by several groups using different techniques [29, 30, 31, 32, 33, 34, 35, 36]. Both the yield as a function of air pressure and the spectrum have been reported at several, often quite low, electron energies.

1.3 The FLASH Experiment

The FLASH (FLuorescence in Air from Showers) experiment is an effort to reduce the systematic uncertainty in energy determination for UHECR fluorescence detectors by making an improved measurement of the fluorescence yield and spectrum. The experiment also explores the energy dependence of the yield in the energy range important for UHECR observation down to lowest energy effective in air showers, ~ 100 keV. In the laboratory, we measure the air fluorescence light directed excited by high energy electron beams or generated in the beam initiated electromagnetic showers, under controllable conditions.

In the first stage of the experiment, we measure the absolute total light yield and the spectrum of the air fluorescence, directly excited by a 28.5 GeV electron beam, over the range of pressures important for UHECR fluorescence detectors [8, 9]. It makes use of a detector calibration technique systematically different from other approaches. The goal is to reduce systematic uncertainties in the fluorescence yield and spectrum below 10%, which is comparable to other current UHECR experimental uncertainties.

A key assumption in the reconstruction of UHECR energy using the fluorescence technique is that fluorescence light is proportional to energy deposition at all depths in the shower. The validity of this assumption should be verified by experiments. It is worth noticing that the energy loss to the air gas is a function of the energy of the charged shower particles, changing rapidly below the minimum that occurs at about 1.5 MeV [23] (see Fig. 1.1). Yet a significant fraction of the energy in an air shower is carried by electrons with energy below 1 Mev and extending down to 100 keV. The fluorescence efficiency in this energy range is poorly known. While the energy lost for these particles is high, their range is short and not well defined. For these reasons, in the second stage of the FLASH experiment, actual showers are generated by electron beams hitting air-like targets with various depths. We therefore examine the precision with which the simulation profile of

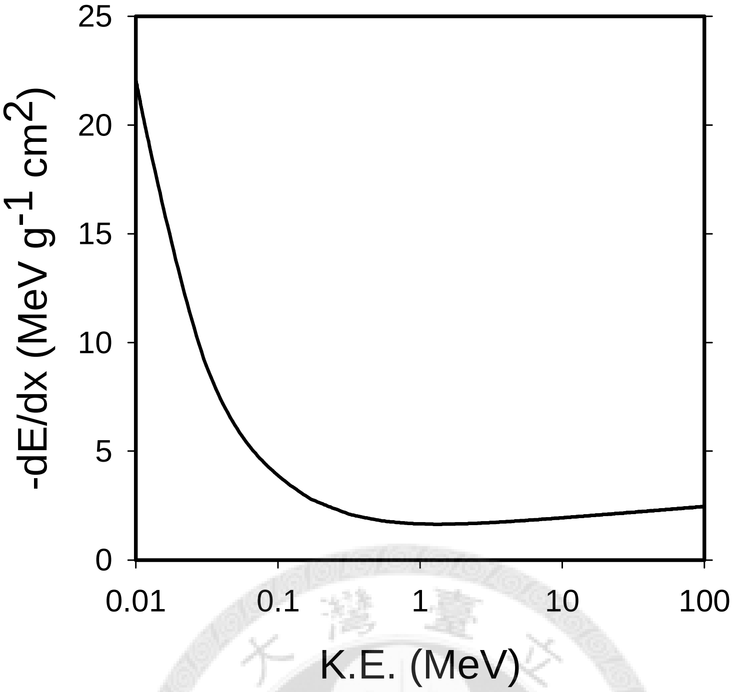

Figure 1.1: Energy loss per unit thickness in air vs. particle energy, from the Bethe-Bloch equation. The energy loss rate changes rapidly below the minimum $\sim$ 1.5 MeV.

shower development and energy loss, and the actual ionization measurements, agree with the profile measured using the fluorescent light [7, 10].

This work is published in Astropart. Phys. [7, 8] and Nucl.Instr. Meth. A [9, 10]. It provide reliable fluorescence information for current and future UHECR experiments using the fluorescence technique, and should help to shed light on the discrepancy between results from different detectors.

Chapter 2

The FLASH Thin Target Experiment[*]

2.1 Experimental method

2.1.1 Overview

This is an experiment to measure air fluorescence yield and spectrum. Many of the previous works measuring the air fluorescence used radioactive sources, whose energies correspond to the low end of the dominant shower spectrum. It entails different systematic issues to use high energy electron beams to excite the air . In this approach, both the electron trajectory and the fiducial light emission length are easy to model. With a short (a few ps) but abundant (up to $\sim 10^9$ electrons) beam pulse, statistics can be quickly collected with negligible dark noise of photomultiplier tubes. However, issues of linearity of the signal response and the radiation backgrounds must be checked and studied. Heavy shielding should be used to reduce the radiation noise.

We use the electron beams available in the Final Focus Test Beam (FFTB) facility at the SLAC National Accelerator Laboratory (see Fig. 2.1) for this experiment. Electrons at 28.5 GeV are delivered at 10 Hz in pulses 3 ps long. The instruments installed for this experiment include a spectrograph for spectral measurement, a toroid for beam charge measurement, the florescence chamber for light measurement, and a beam spot monitor for beam profile measurement. The fluorescence chamber is installed in an air

---

[*] This work has been published in Astropart. Phys. and Nucl. Instrum. Meth. [8, 9].

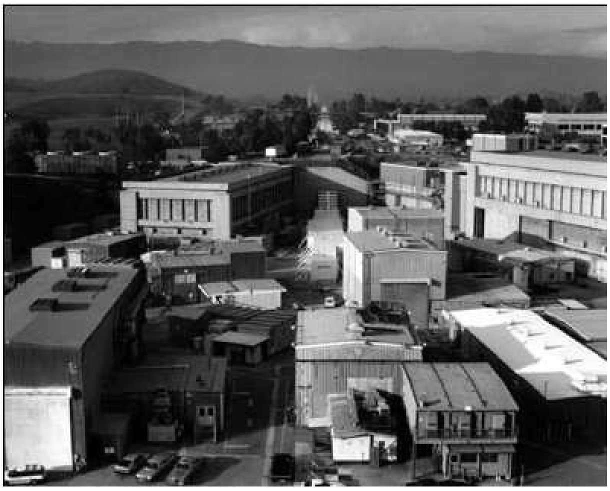

Figure 2.1: SLAC research yard. In the center is the Final Focus Test Beam facility.

gap between the beam vacuum lines, downstream of the last magnets. The upstream and downstream beam windows are made of 50 micron thick stainless steel. The other instruments are installed nearby along the beam line. The beam is focused effectively at infinity in this region.

2.1.2 Beam Profile Measurement

The transverse distribution of the beam is measured nearby the fluorescence chamber using optical transition radiation emitted from a titanium foil in the beam (see Fig. 2.2). This light is reflected by a mirror to allow better shielding. Images are captured by a CCD camera [37] and image capture system. A computer necessary for the system is placed inside the FFTB tunnel with heavy shielding (see Fig. 2.3). The images are stored in the computer but the profiles are made and are accessible to us and the SLAC Main Control Center instantly. This system works as the real-time beam spot monitor (see Fig. 2.4) to help us control the beam positions and sizes throughout the experiment. Both the quality and stability of the beam are essential to reduce the background noise in this experiment. The beam size is also a factor for the linearity of the fluorescence signal response to the beam charge. The Beam spot widths are set to be $\sim$1 mm (see Fig. 2.5).

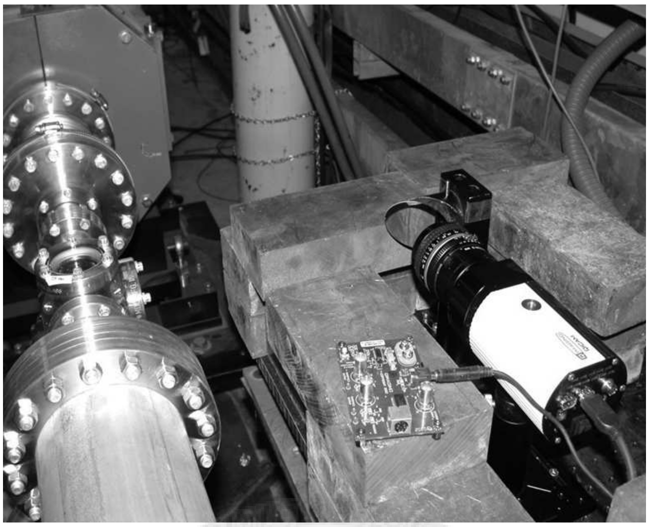

Figure 2.2: Apparatus of the beam spot monitor using the optical transition radiation technique. The light emitted from the titanium foil installed inside the six-way vacuum tube in the beam line is reflected by the mirror and captured by the CCD camera.

Figure 2.3: The computer inside the shielding is used for the beam spot monitor.

Figure 2.4: Real-time display of the beam spot profiles.

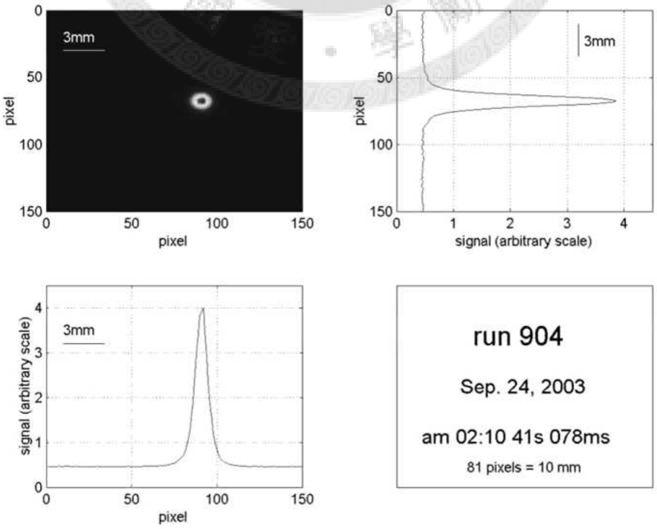

Figure 2.5: The beam image and profiles of a typical event. The sizes of the beam spots are typically around 1 mm × 1 mm.

2.1.3 Beam Charge Measurement

The amount of air fluorescence light directly track to the incident beam intensity. The light signal should be divided by the absolute beam charge in each pulse for deducing the fluorescence yield. Nonlinearity should be studied and only data in the linear region would be used for the yield deduction. For these purposes, a toroid is mounted in the beam line upstream of the fluorescence apparatus [38]. A ferrite-core toroidal current transformer technique is used. The electron beam passes through the ferrite ring which has an evenly spaced copper winding. The current pulse induced in the winding is sent to a front-end amplifier, which is mounted close to the beam line. A bandpass filter is used to improve the signal to noise ratio. The filtered signal is sent to the remote data acquisition system approximately 100 ft away. The signal is digitized on each beam pulse by an 11-bit ADC and read out by a computer. The toroid has a large dynamical range from 10^7 to 10^9 electrons per pulse. The resolution is approximately 1% at the lowest current and 0.2% at the highest current. This unit is calibrated using the charge injection method. This method mimics the current induction process occurring in the beam environment by injecting known charges into the toroid. Long-term stability is monitored using calibration data taken in-between beam pulses during the experiment. The overall uncertainty is found to be better than 2.7%. Details of the design and calibration of this instrument can be found in Ref. [38]. Note that the toroid is mounted only upstream of the fluorescence chamber. The perturbation on the electron flux caused by the thin beam windows should be evaluated by simulation.

2.1.4 Fluorescence Light Measurement

The amount of air fluorescence light emitted in a defined length of track is measured in the fluorescence chamber (see Fig. 2.6 for a illustration of the apparatus). The apparatus consists of a 25 cm long, 15 cm diameter cylindrical gas vessel made of stainless steel. Along the beam line, the upstream and downstream pressure windows are both made of 25 micron thick aluminum. Inside the vessel, a pair of 1.6 cm diameter, thin and blackened, aluminum tubes are placed coaxially with the beam, with a gap of 1.67 cm between them in the center of the volume. This gap defines the length of light emission track to be observed by the photomultiplier tubes (PMT). The internal surfaces are coated black to suppress scattered light, including the forward-emitted Cherenkov radiation.

There are two light channels extended out from the gap radially through the cylinder walls. The two channels, labeled as North and South based on their geometry around the beam line, are at right angles to each other. Their interiors are coated black and heavily baffled against scattered light. Each channel terminates at 45 cm from the beam axis, with a 1.2 cm diameter fused silica pressure window. The light continues on for 15 cm, undergoing a right angle reflection at a UV enhanced aluminum coated mirror before reaching the PMT. This turn allows heavy lead shielding to protect the tubes form direct scattered radiation from the beam line. A remotely rotatable filter wheel is installed in front of the PMT. Filters including a sample of the 300 - 400 nm filter used in the HiRes telescopes, a clear aperture, a opaque filter and various narrow band filters are used.

The fluorescence light is collected by one photomultiplier tube (38 mm diameter Photonis XP3062 [39]) in each light channel. The high voltage is monitored throughout the experiment. Ultraviolet LEDs, flashed between electron pulses, are used to monitor the stability of PMT gain. One is mounted diametrically opposite of each light channels in a shorter baffled cylinder. Four others are placed between the filters and the PMT face, outside the optical path. In the same shielding enclosure, a “blind” PMT is placed with its photocathode hooded. This is used as a background counter monitoring noise from penetrating radiation. An additional hooded tube with a different gain is placed in a separate shielding enclosure nearby.

A gas system outside the beam radiation enclosure can fill the fluorescence chamber with selected pressured dry air. Ambient moist air can be used to investigate the effect of water vapor. For systematics checks, pure nitrogen which fluoresces more strongly than air, or ethylene which fluoresces very weakly can be used. The pressure setting varies in steps in the range from 10 torr to 750 torr.

A standard CAMAC gated analog-to-digital-converter (ADC) system controlled by a computer is used to record signals form the PMT and the toroid. The gas pressure, filter

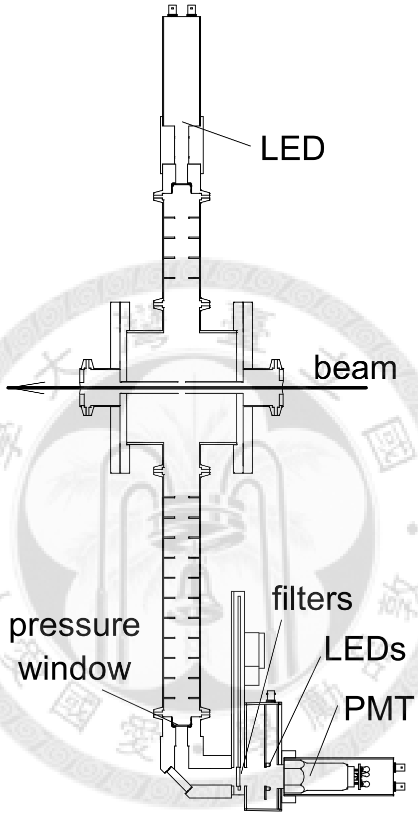

Figure 2.6: Apparatus for fluorescence measurement. The electron beam axis is indicated by the arrow. The optical path is perpendicular to the electron beam along a baffled tube, through a fused silica pressure window, to a right-angle reflection. Following this is a filter wheel, LEDs (outside the fluorescence light path) for monitoring PMT gain stability, and then the PMT for light collection. An LED also for stability monitoring is mounted diametrically opposite of the light channel.

position, PMT high voltage, temperature, and gas humidity are also recorded. During the beam runs, occasional triggers are imposed to measure ADC pedestals and to pulse the LEDs for PMT gain monitoring. Calibration of this system is described in 2.2.

2.1.5 Spectrum Measurement

The spectrum is needed for actual calibration in the cosmic ray shower measurement to take account of filter transmission and PMT quantum efficiency, and the wavelength-dependent Rayleigh scattering. For this reason, a spectrograph system with relatively high resolution is installed separately in the beam line for relative spectral measurement. In a thin-windowed and baffled gas cell, fluorescence light is emitted from the beam axis, passing through an defined aperture, reflected by two aluminum-coated mirrors, through a fused silica pressure window and a focusing mirror, and arrives the heavily shielded spectrograph [40]. Signals are measured pulse by pulse by using a 32-anode PMT [41]. The anode signals are digitized by the standard CAMAC 11-bit ADCs. Background is measured by deflecting away the light path away from the spectrograph slit. This system is not synchronized with the toroid. Signals are average over each data run at a fixed pressure, with the background and the ADC pedestal subtracted.

Calibration of the system is carried out off the beam line. The wavelength settings are determined by the positions of the lines from a mercury discharge lamp. The wavelength-dependent sensitivity is studied by recording its response to a deuterium lamp with continuous spectrum. An uncertainty of $\sim 15\%$ in the relative light yield of the short wavelengths $\sim$ 315 nm, relative to the rest of the spectrum which extended to 415 nm is found. In addition, a correction of the nonlinearity of anode signals for the strong lines is studied. An average systematic uncertainty of 17% of this correction is assigned. A smaller uncertainty of 3% accounting for the crosstalk between neighboring anodes is also assigned. Details of the design and calibration of the spectrograph system can be found in Ref. [8].

2.2 Optical Calibration of the Fluorescence Chamber

Optical calibration to translate ADC counts into the amount of light emitted in the defined track length is carried out in a laboratory after the experiment. The fluorescence chamber is moved from the beam line to the laboratory with the vacuum windows replaced by coated optical windows. End-to-end calibration using Rayleigh scattering of laser light is performed for the absolute calibration. The relative calibration of wavelength dependence is performed by using a broad-band mercury lamp as a light source for a monochromater. Details of the this calibration can be found in Ref. [9]

2.2.1 Absolute Calibration

End-to-end calibration takes account of all contributing factors in the system at once. It measures ADC counts responding to know light emission. The calibration takes place in an environmental chamber where the temperature is kept at the average temperature measured in the FFTB tunnel at SLAC. The $\sim 160\mu J$, 4ns beam pulses are injected at a few Hz into the fluorescence chamber along the electron beam axis from a nitrogen laser [42]. The 337 nm laser photons are scattered from the air molecules in the 1.67 cm gap, through the optical path, and collected by the PMT. The PMT signals are digitized with the same ADC system used at the beam line. The energy of the laser beam is measured by a pyroelectric probe [43], which is calibrated by the manufacture to 5%, simultaneously with the PMT signals. The uncertainty of the laser energy is the largest single contribution to the light yield uncertainty. By comparing the PMT responses to the build-in LED flashing between electron beam line setting and the laser beam setting, a 2.5$\%$ stability uncertainty is assigned. The Rayleigh scattering efficiency is calculated based on Ref. [44, 45] with 0.2$\%$ theoretical uncertainty.

Measurements are made at various pressures between vacuum and atmosphere. A linear fit

$$\frac{N_{ADC} - N_{ped}}{E} = G\frac{SP}{T} + k_0 \tag{2.1}$$

is performed to the data, varying the parameters G and k_0. N_{ADC} is the signal counts, N_{ped} is the pedestal counts, E is the laser pulse energy, P and T are the pressure and temperature measured in the chamber, S is the expected Rayleigh scattering rate, and k_0 accounts for the scattering light background. After the chi^2 minimization, G represents the calibrated number of ADC counts per isotropically emitted photon per meter at 337 nm. Data taken at 12 different pressure points for the clear aperture is shown in Fig. 2.7. It is found that the signal strength, normalized to the laser intensity, rise linearly with pressure, as expected from Rayleigh scattering. The intercept at the vacuum setting corresponds to the background from scattered laser light. The slope represents G.

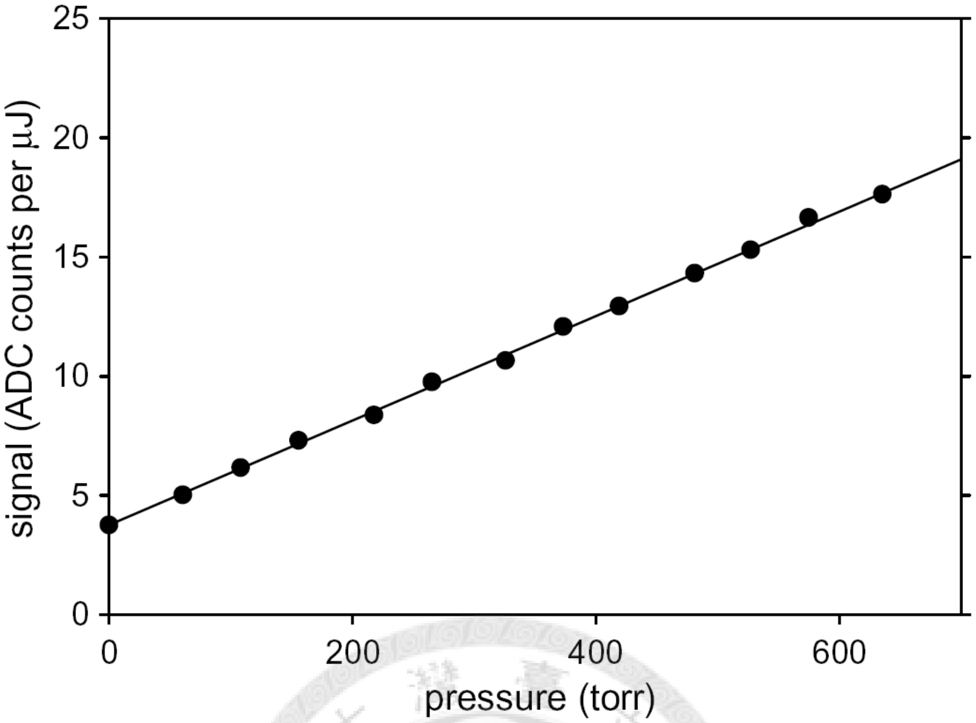

Figure 2.7: PMT response against Rayleigh scattering intensity at various pressures from vacuum to atmosphere. The ADC counts are pedestal subtracted, normalized by the laser power, and averaged at each pressure setting.

Uncertainty taken account for possible thermal differences associated with radiation shielding contributes 1.1%. The uncertainty of the slope fit is 0.2%. Transmission efficiency of the HiRes filter at 337 nm is made by comparing the signal from that using the clear aperture and that using the HiRes. It is compared to results from spectrophotometer measurements performed before the installation of the apparatus at SLAC. A systematic uncertainty of 1.8% is assigned because of this filter consistency check.

2.2.2 Relative Calibration

The calibration is extended to 300 – 420 nm from relative measurements of known monochromatic light. A broad-band mercury lamp as a source for a monochromator with a precision of 0.5 nm is used for this purpose. The light from the monochromator is measured by both the PMT and the NIST wavelength-calibrated photodiodes (Si PDs) [46], wavelength by wavelength (see Fig. 2.8). The PMT response relative to that at 337 nm is shown is Fig. 2.9. For the contribution from wavelengths beyond the limits of the monochromator survey, of a few percent level, the response curve is extended using manufacturer's data. The overall sensitivity to the air fluorescence spectrum is computed using two examples of measured spectra, from the Airfly collaboration [34] and from this experiment. 1.2% overall uncertainty of the relative PMT response is assigned.

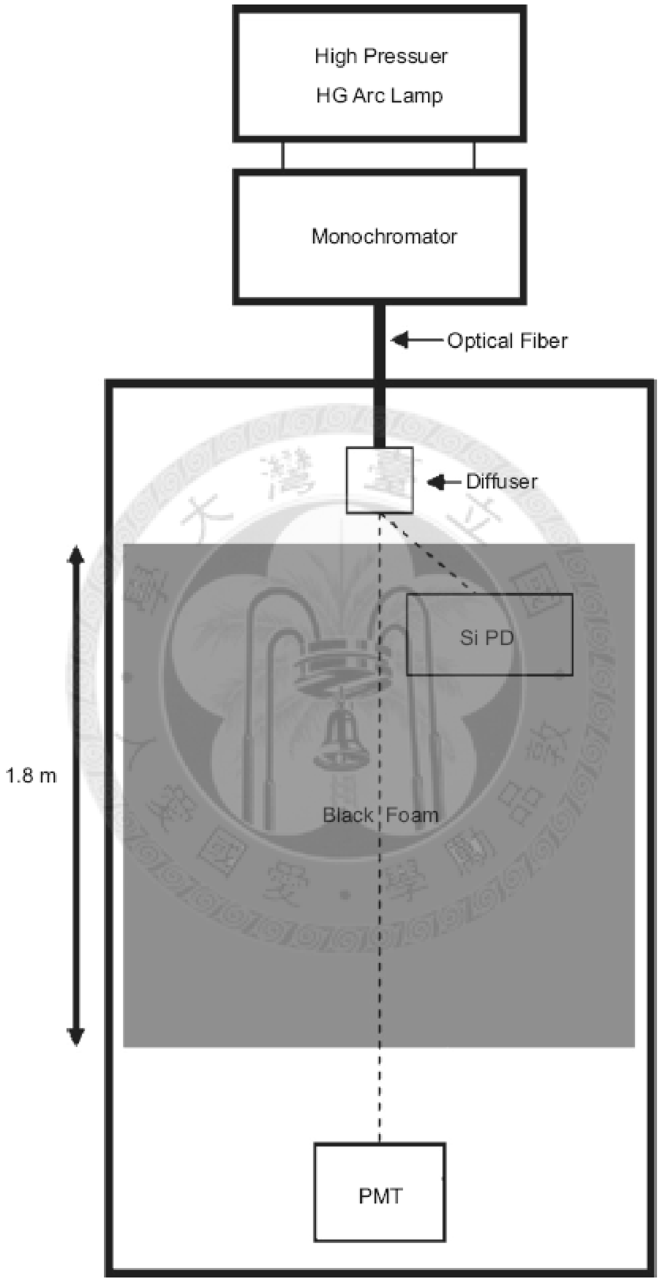

Figure 2.8: The relative calibration setup. Light form the monochromator with a mercury lamp as source is measured by the PMT and the photodiode.

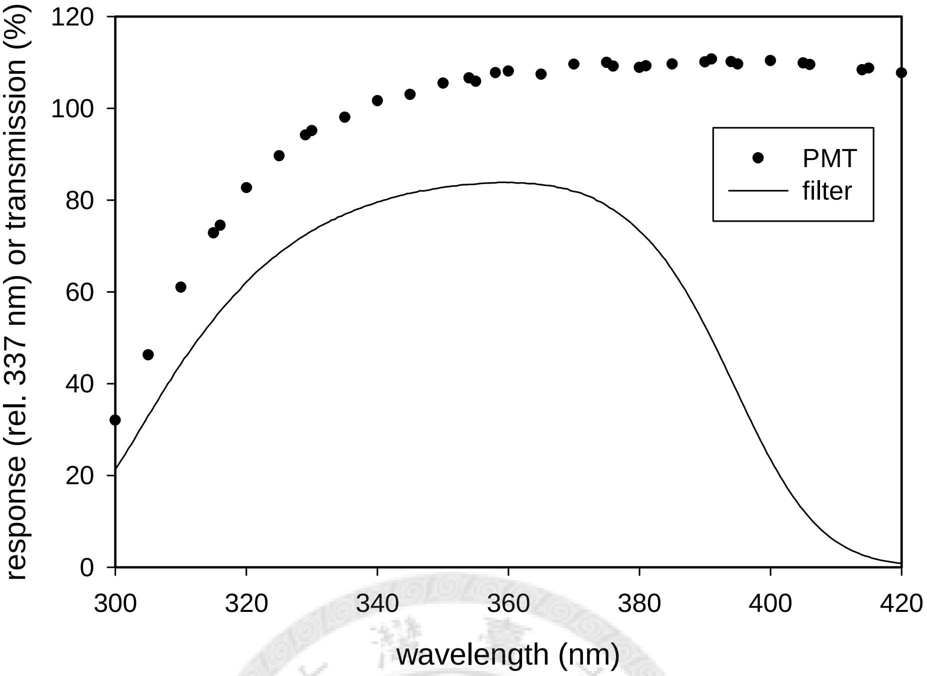

Figure 2.9: PMT response relative to that at 337 nm, and transmission of HiRes filter, vs. wavelength. It varies by less than 10% between 337 and 420 nm. At 300 nm it is 30% of the 337 performance.

2.2.3 Acceptance and Energy Deposit Correction

A correction is applied to take account for the geometry difference between the light source from localized laser Rayleigh scattering and that from the more wide-spread energy deposition from the electron beam. The spread of the energy deposited by the electron beam in the apparatus is simulated using EGS4 [47]. The acceptance efficiencies at the optical iris are numerically calculated for both the laser and electron beam cases. The efficiency of converting photons to ADC counts from the laser case is found to be (3.2±0.25)% more than that from the electron beam, in the apparatus fiducial volume. In addition, the ratio between the energy deposited in a 1 cm length of free air without beam windows and that in the fiducial volume is 1.0837 ± 0.0015. For calculations using the actual energy deposit in the fiducial volume, an overall simulation systematic uncertainty of 1% should also be applied.

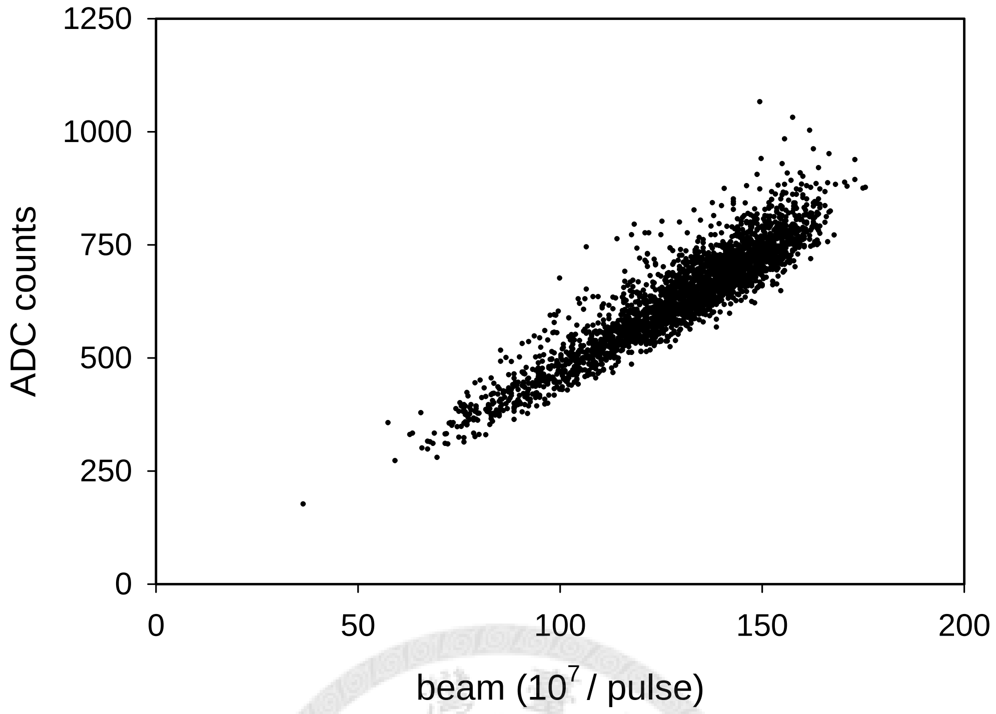

Figure 2.10: Pedestal subtracted signals plotted pulse-by-pulse against beam intensity at 750 torr, using HiRes filter.

2.3 Data Analysis and Results

2.3.1 Data Processing and Background Subtraction

The data are collected in runs at selected settings of pressure and filters. There are several thousand beam pulses in each run. ADC pedestals are measured occasionally in between electron pulses. Signals from the signal PMT and the background PMT (blinded) are plotted against beam charge, pulse by pulse (see Fig. 2.10 for example). Background runs with opaque filter in position are interspersed among others. The fluorescence signals are obtained after both the pedestal and the background being subtracted. The background, typically $\sim 5\%$ for data without a filter, is obtained from nearby opaque filter run, and is corrected with a run-to-run background ratio measured by the blinded tubes. Only the results of the north PMT are to be discussed here. The south PMT, with a higher gain selected for narrow band filter measurement, is in saturation for relatively transparent filter configurations. The narrow band filter results are intended to be the subject of a future report.

In the intended low beam intensities runs, the intensities typically vary by $\sim \pm 30\%$. This permits the signal vs. charge plot to be studied for systematic effects. The regression of the data in those runs is found to intersect the charge axis at $(-0.41 \pm 0.31) \times 10^7$ electrons per pulse. This offset is applied to all subsequent fits, where the typical beam intensity is $\sim 10^9$. A conservative contribution of 1% is included in the overall uncertainty evaluation. Linearity of the signal response to the beam charge is studied whereas two effects are observed. The first is the PMT saturation, which affects a small fraction of high pressure data where no optical filter is used. The second is the non-linear effect caused by the collective electric field impulse of the intense electron bunch. This field accelerates electrons freed by ionization events, and these electrons in turn cause more molecular excitations to generate additional fluorescence light. Related effects have been studied in the same beam line [48]. This enhancement of the fluorescence is illustrated in Fig. 2.11. We find that for beam spots $\sigma_x \times \sigma_y$ of 1 mm $\times$ 1 mm, and 1 mm long, the beam intensity threshold for the enhancement decreases with gas pressure, from 1.5×10^9 at 1 atm to 0.8×10^9 at 50 torr. Nonlinearity from these two effects is avoid by imposing cuts to beam intensity in the corresponding runs.

Most of the data sets are taken in the 2003 beam run. We retake some of the settings again in the 2004 beam run. The repeatability of the results between the two beam runs is tested by comparing data sets taken under similar conditions. An uncertainty of $\pm 2\%$ is assigned from the observed variations.

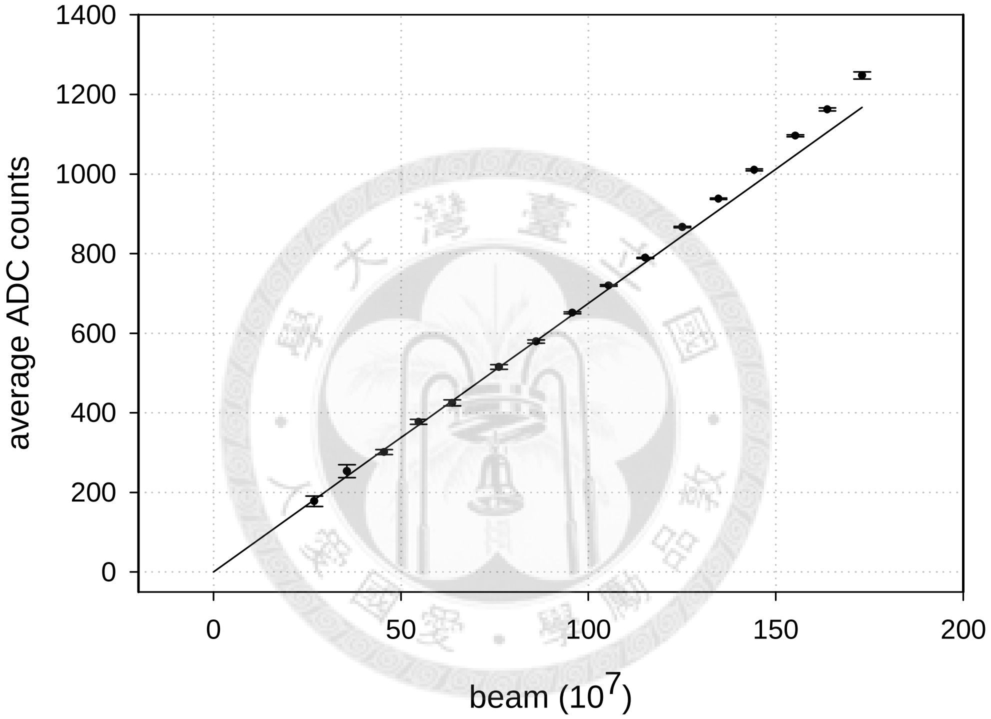

Figure 2.11: Fluorescence signals plotted against beam intensities at 250 torr with no optical filter. The enhancement induced by the collective electric field impulse occurs at higher beam intensities.

Table 2.1: Photons per MeV as measured with no filter and with the HiRes-filter. An overall uncertainty of 7.5% applies to the yields (see text and Table 2.3 for details)

	photons / MeV	
pressure (torr)	no filter	through HiRes filter
750	20.8	14.0
495	32.0	21.7
242	64.3	43.0
97	157.6	105.2
50		182.2

Table 2.2: Photons per electron-meter for no filter and HiRes filter cases. The relative uncertainty between points at different pressures is 1.42%, and an overall scale uncertainty of 7.5% applies to all points.

pressure (torr)	no filter	HiRes filter
750	5.059	3.413
495	5.029	3.403
242	4.848	3.240
97	4.686	3.128
50		2.784

2.3.2 Photon Yield in Dry Air

Several runs are separated taken for each setting of pressure and filter. The results from separated runs at each setting are averaged since they show very good consistency. The variation between them is used to estimate a run-to-run uncertainty. Based on this, a 1% uncertainty is assigned.

After applying the calibration discussed in Sec. 2.2, the dry air results are given both as photons per Mev and photons per electron-meter in Table 2.1 and Table 2.2, at some pressures in the range of interest for UHECR fluorescence detectors. Only HiRes filter data are available at 50 torr. The uncertainties that should be applied to these values are listed in Table 2.3 in units of percent. The overall uncertainty is 7.5%. The fluorescence yield at 750 torr and 304 K is reported as 20.8 ± 1.6 photons per MeV.

The HiRes filter results are plotted in Fig. 2.12. This shows that the air fluorescent yield barely increases with pressure above ~ 0.1 atm. This is because that increasing collisional de-excitation compensates the increasing energy deposit with gas density. The

Table 2.3: Contributions to uncertainty on the photon yield, in units of percent

uncertainty contribution	%
beam calib.	2.7
signal splitter	1
zero constraint of fits	1
run-to-run stability	1
laser vs e-beam light source shape	0.4
simulation	1
spectrum sensitivity, open filter	1.5
spectrum sensitivity, HiRes filter	1
beam line vs lab stability	2.5
2003 data calib.	2
filter consistency checks	1.8
PMT relative spectral response	1.2
Rayleigh scattering:	
laser power	5
gas density for laser scattering	1.1
theoretical calculations	0.2
fit slope	0.2

fit line in the figure is the expression $aP/(1+bP)$ [24, 31] motivated by quenching of the fluorescent molecules by pressure dependent collisions, where P is pressure and a, b are fitting parameters. The error bars shown in the plot are the point-to-point relative uncertainties of 1.42%. The overall 7.5% scale uncertainty still applies to all points. Results from using other gas composition are not discussed here but can be found in Ref. [8].

2.4 Fluorescence Spectrum

Results from the narrow band filters are still under studied and will be reported in the future. Here we present the spectral results from the spectrograph. The fluorescence spectrum is measured at various pressure settings. As an example, Fig. 2.13 shows the spectrum measured at 155 torr, where each bin ($\sim$4 nm) corresponds to one anode and the sum of the bins is unity. The relative signal strengths in several wavelength ranges are shown in Fig. 2.14 at various pressures. There is no strong change in the spectrum oabove $\sim$100 torr. Calculations show that the transmission efficiencies of these spectra through

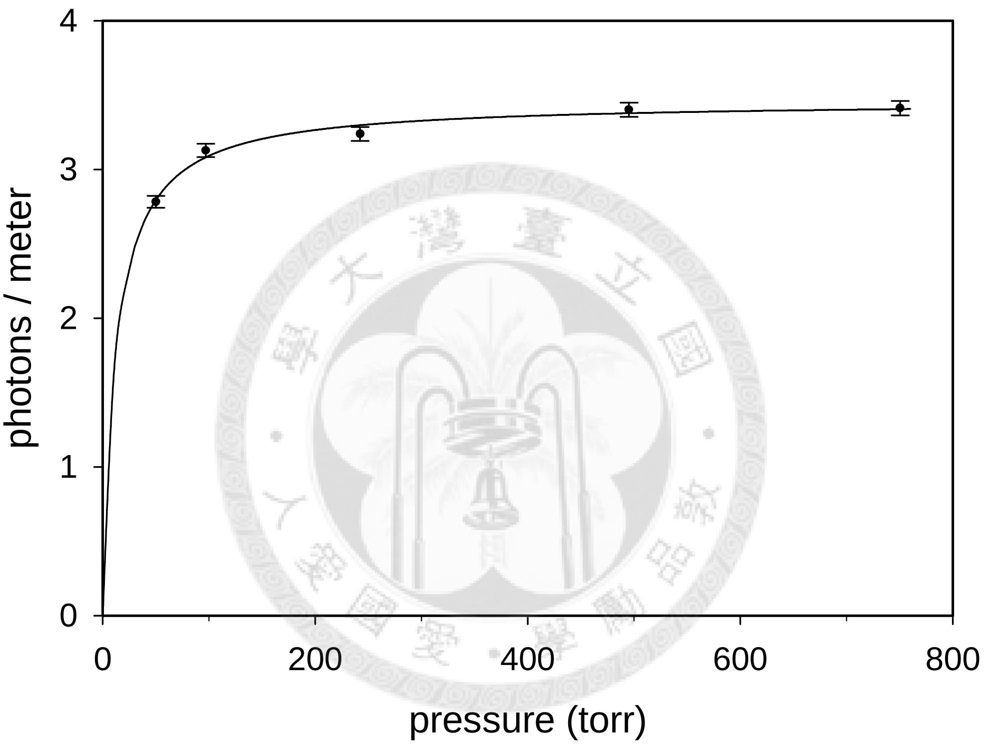

Figure 2.12: Photons per meter-electron measured using the HiRes filter. The error bars shown indicate the point-to-point uncertainty of 1.42%. An overall scale uncertainty of 7.5% applies to all points. The fit expression is $aP/(1 + bP)$ (see text for explanation.

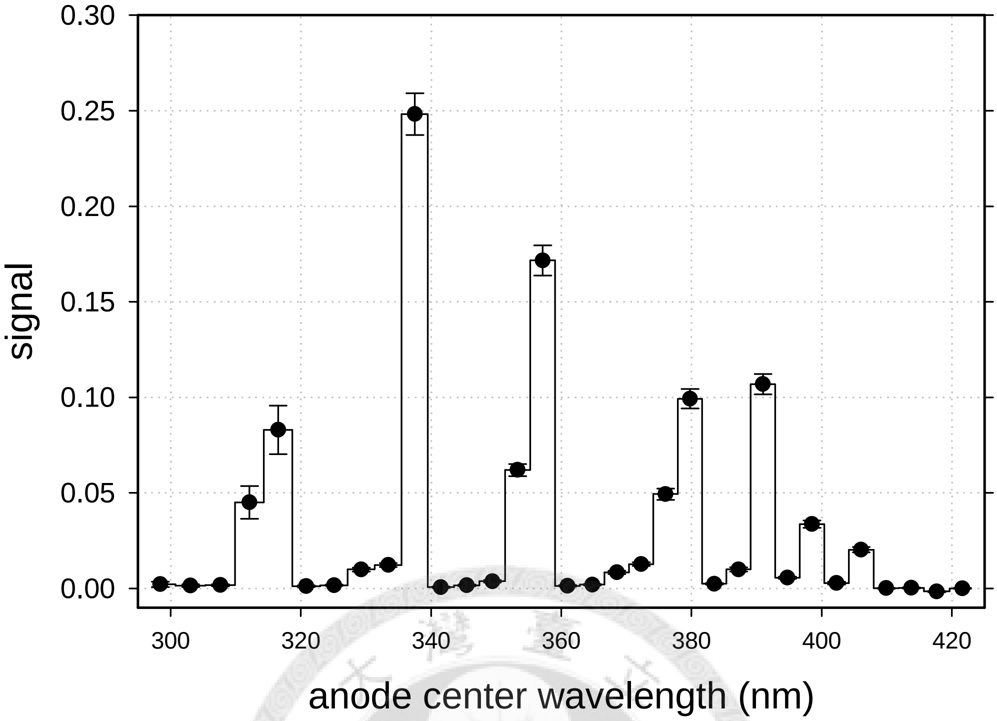

Figure 2.13: Fluorescence spectrum of 155 torr air observed by using the 32-anode PMT. Each bin corresponds to one anode and the sum is normalized to unity. Corrections for transmission, conversion efficiency and non-linearity have been applied.

a HiRes filter vary by 0.46% rms, whereas the largest deviation from the mean is 0.70%. Also, the transmission efficiencies taking account for the Rayleigh Scattering through 30 km of 1 atm. air varies by less than 1% for the spectra at pressures above 60 torr. The 391 nm line is observed to become relatively more important as pressure decreases below 60 torr. This is also expected by theory [26] because of the differences in the radiative and collisional de-excitation rates of the corresponding quantum state.

The response profile across the 1 mm width of each anode rises and falls between the inter-anode gaps. Numerical calculation taking account for this profile is performed to translate the “spectrum” of anode signals to that of emission lines. The air fluorescence spectra for resolved emission lines between 300 and 415 nm are obtained by matching known lines with the response profile in the calculation. As an example, the result at 155 torr, is illustrated in Fig. 2.15, where the line strengths are expressed as a fraction of the total yield in the full wavelength range.

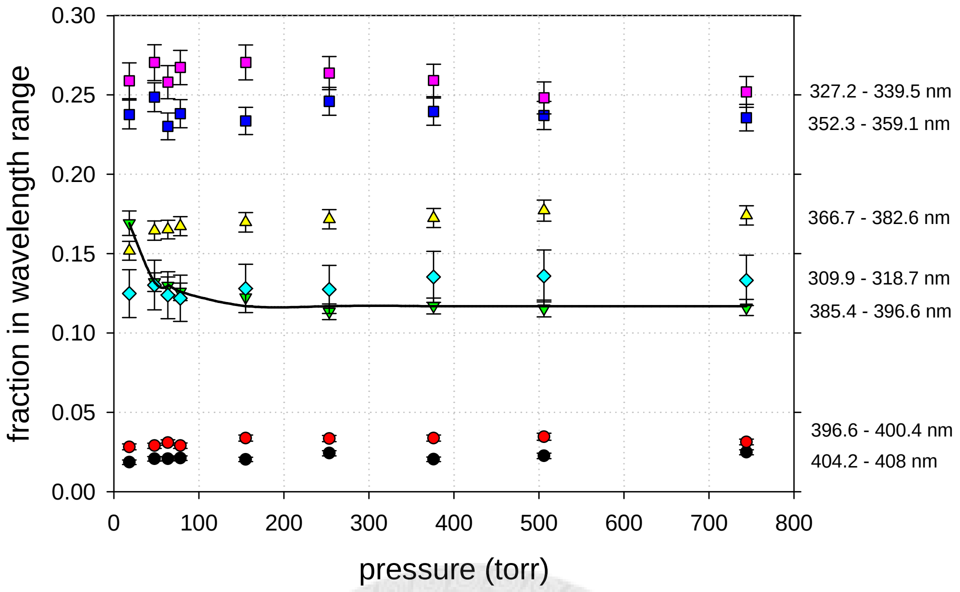

Figure 2.14: Pressure variation of the relative contributions of various wavelength ranges. The most noticeable structure is the rise below 60 torr of the fraction of light in the 391 nm band, illustrated by the line.

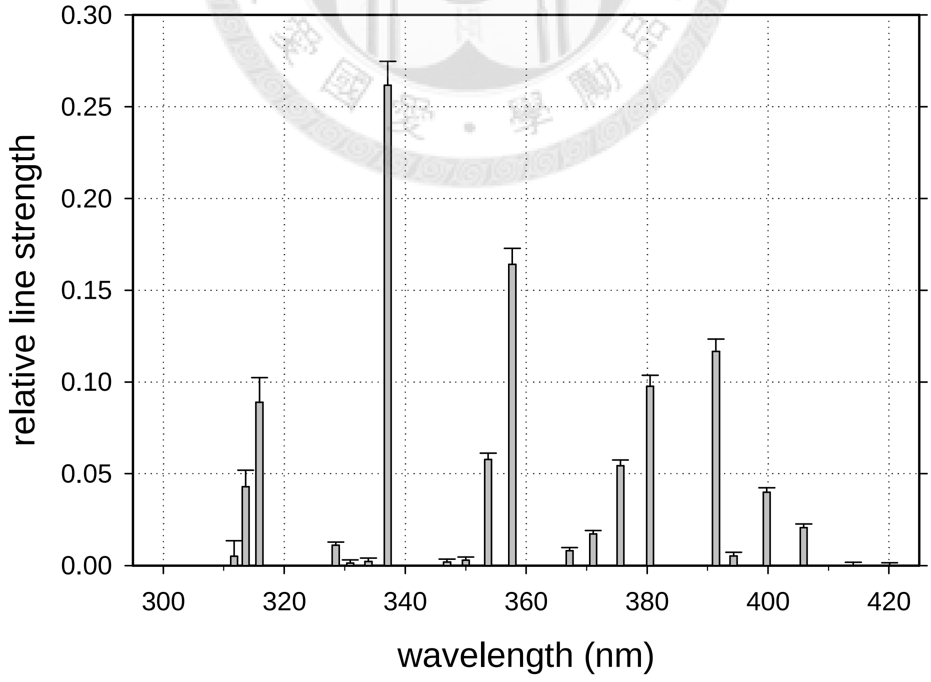

Figure 2.15: Line spectrum from 155 torr air, obtained by matching known lines with the response profile of the spectrograph. The sum of the line strengths is normalized to unity.

2.5 Conclusion and Discussion

We provide reliable and relatively precise information, based on experiment, of the both total and spectral fluorescence light yield for the use by UHECR fluorescence detectors. The uncertainties have been assigned in a conservative manner. Repeatability has been checked by re-performing some of the settings a year after the main data run, and the resulting variation has been included in the overall uncertainty. The 7.5% overall uncertainty of the total yield is mainly contributed by the uncertainties of the toroidal and the optical calibrations. The calibration techniques can in principal be further developed to meet the more stringent demands of future UHECR measurements.

The total yield result agrees with those published in Ref. [32] and [33] within the uncertainties, if we take account of the temperature-dependent quenching effect represented as a modification in the denominator of the expression in Sec. 2.3.2: $aP/(1 + bP(T/304)^{1/2})$ [24, 31].

The observed spectrum shows that the emitted fluorescence light indeed comes from the expected nitrogen bands [24, 28]. Although there are discrepancies in detail, general agreement is found in comparing with other reported spectra. Various reported emission strengths are illustrated in wavelength bands for the range 300 to 420 nm in Fig. 2.16. Reports from the early work of Bunner [24], the optical filter work of Nagano and collaborators [30], the Airfly collaboration [34] and from this paper, are shown for comparison in the same bands. In each case, the plotted values are expressed as a fraction of the total emission reported within the range. The total transmission efficiency of the HiRes optical filter for these spectra is the same within 1%. As for the wavelength dependence of Rayleigh scattering, the transmission values are calculated for these four spectra through 10 km air at 1 atmosphere. They average 0.481 with a worst case deviation from the mean of 0.009. Through 20 (30) km at 1 atm, the average transmission is 0.242 (0.124) with a worst case deviation of 0.008 (0.009). The agreement is adequate for the UHECR data analysis at the present experiment accuracy level. However, the transmission differences amounting to up to 7% at 30 km atm will become significant for future UHECR detectors, which have farther sighting ability and better accuracy. The differences of the

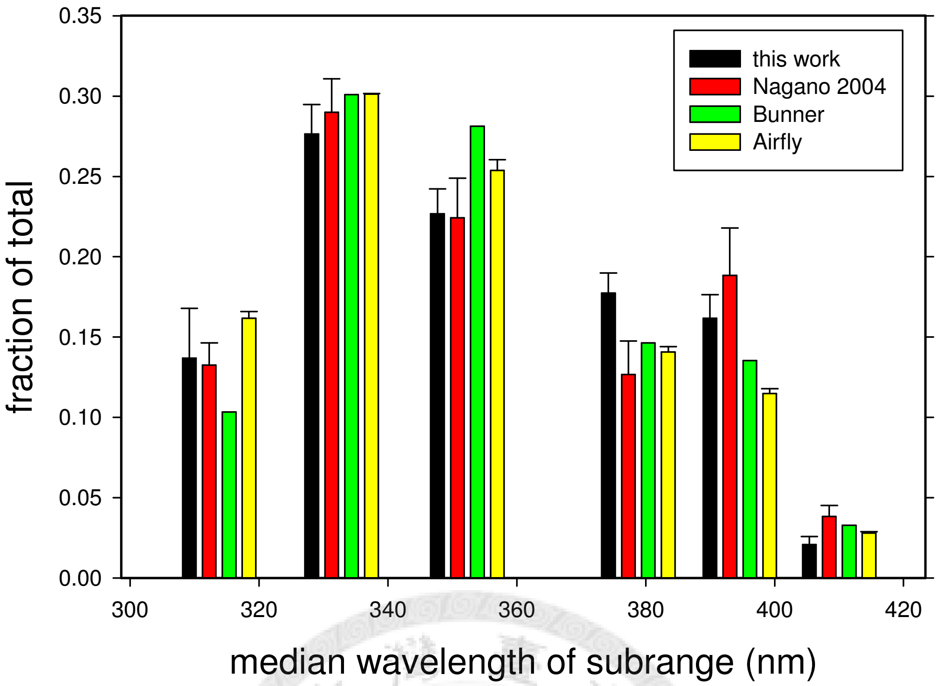

Figure 2.16: Comparison between reported emission strengths and those reported here, grouped into six wavelength bands, for the range 300 to 420 nm. Minor adjustments have been made to allow for compatible wavelength ranges. In each case the sum of emissions is normalized to unity.

spectral results will then need clarification.

The recalibrated UHECR spectrum based on the measurement from this work and the differences of that based on other reported measurements should be further studied and reported in the future.

Chapter 3

The FLASH Thick Target Experiment[*]

3.1 Experimental Method

3.1.1 Overview

This experiment is a study of the longitudinal profile of electromagnetic shower initiated by the electron beam at the SLAC FFTB facility. It studies the shower profile in the energy range relevant to UHECR shower measurements. Electrons at 28.5 GeV are delivered at 10 Hz in 5 ps long pulses. Each pulse contains a few $\times 10^7$ particles. The effect of the electron energy is only to affect linearly the total energy deposit, since the shower energy deposited is primarily contributed by the electrons with energy below $\sim$100 MeV. The effective particle spectrum at each shower depth is not significantly affected by the initial energy. However, the material in which the shower develops, affects the shower's ratio of width to depth. It also determines the critical energy, below which the energy loss is dominated by ionization rather than particle production.

The strategy of this experiment is to produce a shower with characteristics similar to an extensive air shower in the laboratory, then measure the fluorescence light emitted in comparison with measured ionization and simulation results at various shower depths. We choose to use the commercially available alumina ceramic as the material in which the shower develops, based on practical and economical reasons. The ceramic is made

---

[*] This work has been published in Astropart. Phys. and Nucl. Instrum. Meth.[7, 10].

of Al_2O_3 with 10% SiO_2, delivered in brick form. The measured mean density is 3.51 g cm^{-3}. The radiation length is 28 g cm^{-2}, 24% less than that of air, and the critical energy is 54 MeV, while it is 87 MeV for air. It is the closest practical approach to simulating air that we encounter for the electron beam energy.

Instruments installed in this experiment include the toroid for beam charge measurement (described in the previous Chapter), the thick-target fluorescence chamber for fluorescence light measurement, the ion chamber for ionization measurement, and a scintillation-screen-camera system for transverse shower profile measurement. We also simulate the shower development using EGS4 and GEANT3 shower simulation codes.

The thick-target apparatus is shown schematically in Fig. 3.1. It is installed in a gap in the electron beam vacuum line. The electron beam exits through a thin vacuum window. The alumina bricks are contained in a line of four aluminum boxes, each of which can be moved on or off the beam line remotely and independently. Each of the upstream blocks is approximately 4 radiation lengths (RL) thick (30 cm). The downstream block is approximately 2 RL thick, by 50 cm wide. The air fluorescence chamber is placed immediately behind the blocks. This arrangement permits thicknesses of approximately 0, 2, 6, 10 and 14 RL to be selected for shower development, immediately in front of the detector. In addition, thickness of 4, 8 and 12 RL can be studied. However, in the latter cases there is a 15 cm air gap in front of the chamber, and the downstream alumina block can only be extracted 6 cm away from the beam center.

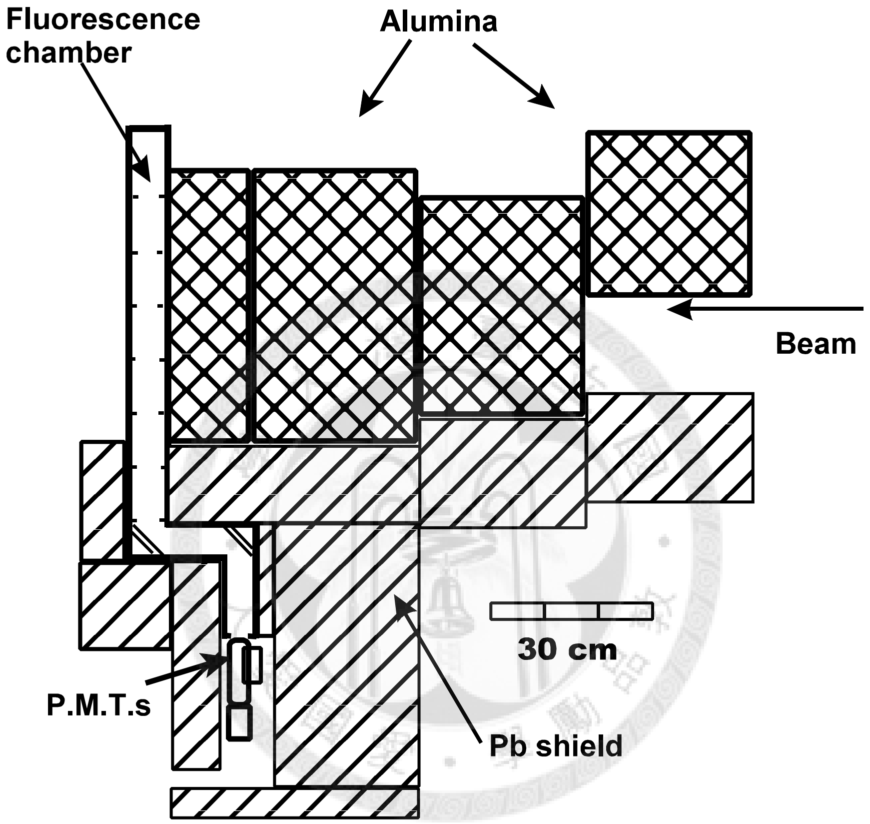

Figure 3.1: Schematic view of the thick-target apparatus. The alumina blocks are shown in the 10 radiation length configuration with the first block moved out of the beam. At left is the air fluorescence chamber. Its doglegged light pipe and PMTs are surrounded by lead shielding. The ion chamber and the scintillation screen can be mounted immediately to the left of the fluorescence chamber.

3.1.2 Fluorescence Light Measurement

The shower particles leave the alumina and enter the fluorescence chamber, where the fluorescence light is emitted in the air at atmospheric pressure (see Fig. 3.1). The chamber consists a flat rectangular aluminum box, which is 6 cm thick and 50 cm wide. In the center of the box are two thinned beam windows with 25 microns thickness and 7.8 cm diameter. In order to suppress the scattering light, including Cherenkov and fluorescence, a set of 1 cm wide vertical baffles on the beam walls are used and the inner surfaces are covered with black flock material [49]. Two right angle turns of the light path are made with mirrors [50] to allow better lead shielding of the PMT from radiation. The minimum thickness of the lead walls is 25 RL.

A total of 6 PMT (XP3062 [39]) in a vertical row are used. Two of them are hooded to track background levels and the other four collect the light signals. The light path can be blocked by inserting a shutter plate into place by hand. In order to estimate the strength of the background radiation, data runs are matched routinely by runs with the shutter inserted. Optical filters including the Hires filter (300 - 410 nm) and bandpass filters can be inserted in the transverse slot in front of the PMT. LED installed on the walls and flashed between beam pulses are used to monitor the PMT gain stability.

The PMT, ion chamber (to be discussed in Sec. 3.1.3), and toroid signals are recorded using a standard CAMAC gated ADC system controlled by a computer. The gate for the PMT is set to 20 ns after the start of the PMT pulses. This timing cut, while retaining the prompt fluorescence signal, excluded signals from penetrating neutrons of energy less than 200 MeV. The PMT high voltages and the temperatures are also recorded. Occasional triggers are imposed to measure ADC pedestals, and to pulse the LED for PMT gain monitoring.

3.1.3 Ionization Measurement

The ion chamber (see Fig. 3.2) can be installed in the space behind the fluorescence chamber for direct ionization measurement. It is designed for the high radiation and ionization levels with wide dynamic range encountered after the shower development. It consists

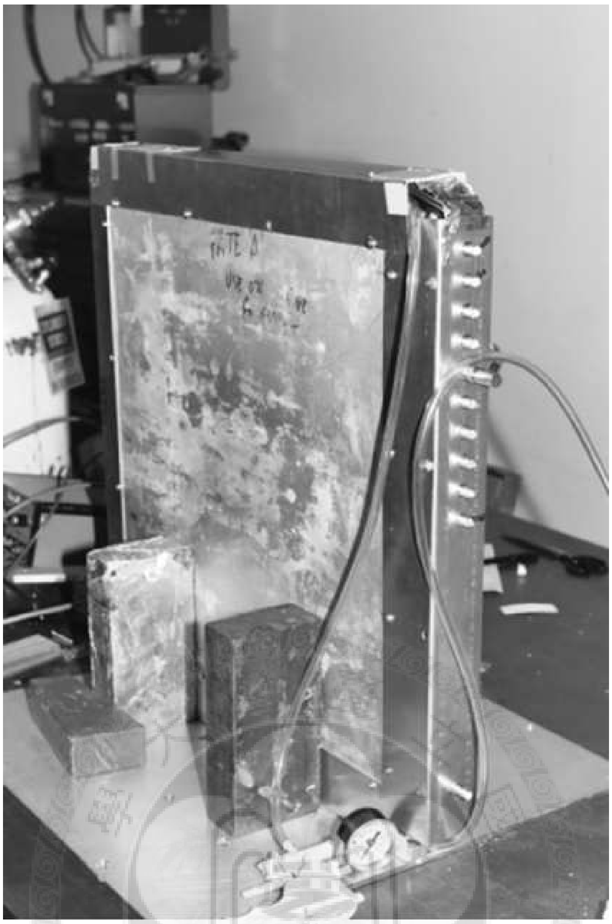

Figure 3.2: Outside look of the ion chamber. The size is about 50 cm. In the inside are 11 gaps filled with helium, separated by plates with high voltage applied.

11 gaps of 0.9 mm thickness, with plates based on printed circuit board covering 50 cm square width. The gas used is helium at 1 atmosphere. The applied voltage of 140 V/mm is chosen to maximize the clearing field and electrode charge without leading to gas gain. All anodes and cathodes are connected electrically. The signals are read out without amplification and recorded by the CAMAC gated ADC system.

3.1.4 Transverse Shower Profile Measurement

A scintillation screen and camera setup can be installed in the same space used by the ion chamber for transverse shower profile measurement (see Fig. 3.3). We use the standard beam scintillation screen, which is made of Cr doped alumina and is 10 cm wide in a square shape. It is taped on the back of the fluorescence chamber. Scintillation light is

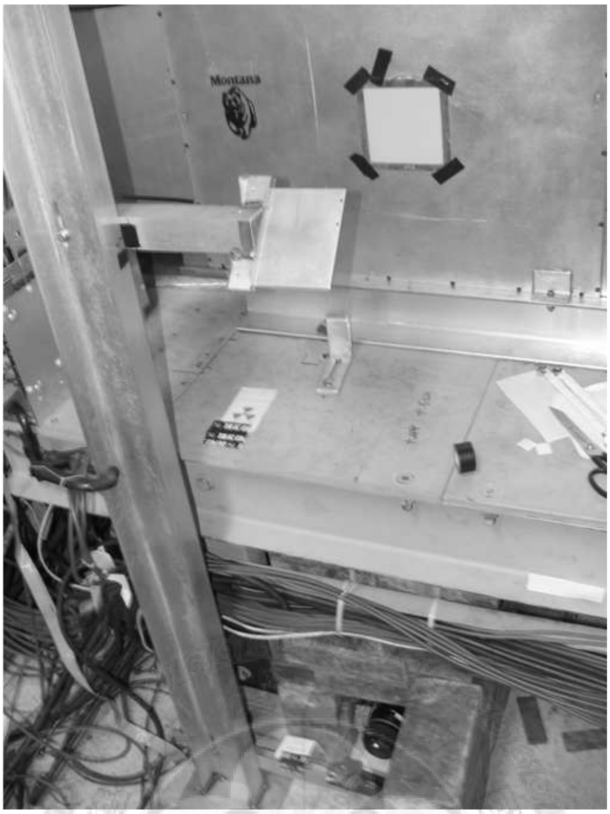

Figure 3.3: Setup of the scintillation screen, mirrors and camera. The 10 cm wide screen is made of Cr doped alumina. It is taped on the back of the fluorescence chamber. Scintillation light is reflected by two mirrors and captured by a CCD camera on the ground.

reflected by two mirrors and captured by a CCD camera, which is sat on the ground and covered with heavy shielding. The image capture system is similar to that used in the thin-target experiment. The data are stored in a computer inside the FFTB tunnel but the profiles are available immediately in the control room. The camera is triggered after the beam arrival in order to get rid of the Cherenkov light. It is found that the scintillation light emission comes from more than one decay channels, some of which have very long decay time. In a single electron pulse test run, a long tail of a few percents of light can still be observed a few tens of minutes after the pulse arrival. For this reason, the screen is removed from the beam line between the screen data runs, and only the first "clean" shower event in each data run is used for the final analysis.

The transverse profile is measured to provide crosscheck on the simulation results and for systematic control. The correct estimate of the transverse shower profile is important for the validation of the design of the apparatus in this experiment.

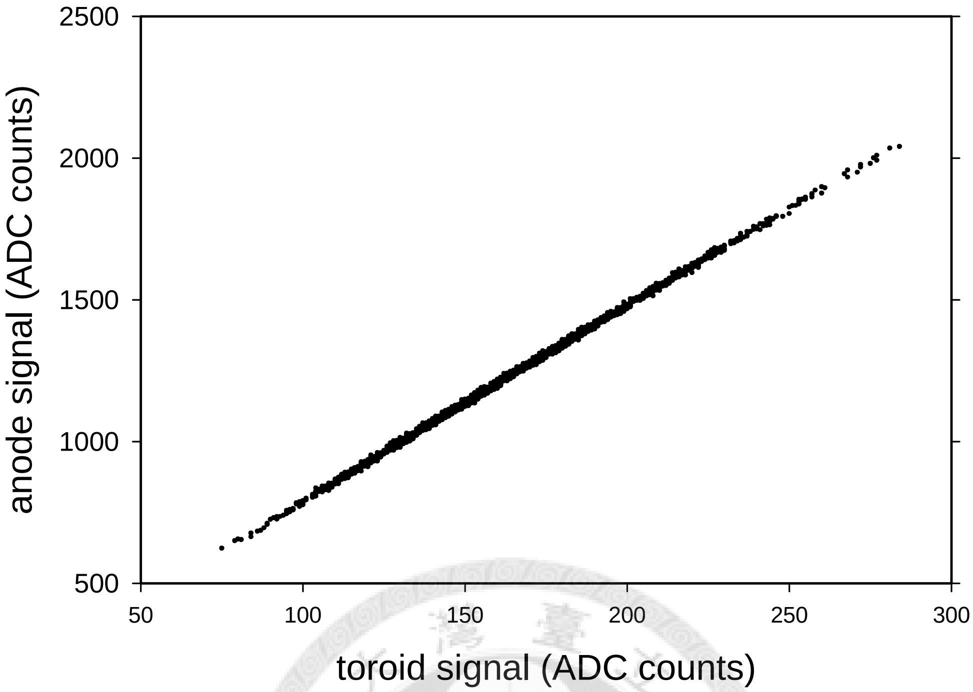

Figure 3.4: Plot of ion chamber signals against beam toroid signals at 6 radiation lengths.

3.2 Data Analysis and Results

3.2.1 Longitudinal Shower Ionization Profile

The ion chamber signals are plotted against the toroid signals pulse by pulse. In Fig. 3.4 is a plot of ionization signals against the toriod signals at 6 RL as an example of this correlation. For the plot at each shower depth, polynomial fits are tested because of concern about nonlinearity occurred at the high intensities in the shower cores. The quadratic fit is selected if the second order coefficient is significant at more than 1.5 standard deviation. The relative ionization strength at each shower depth is realized as proportional to the coefficient of the linear term in the fit.

The resulting longitudinal shower profile, from $\sim$0 to 14 RL, is shown in Fig. 3.5. The signals are normalized to sum to unity. The profile of energy deposit is also studied using EGS4 shower simulation code [47]. An independent study using the Geant3 code [51] gives consistent results. All of the upstream beam window, the air gaps, the boxes of

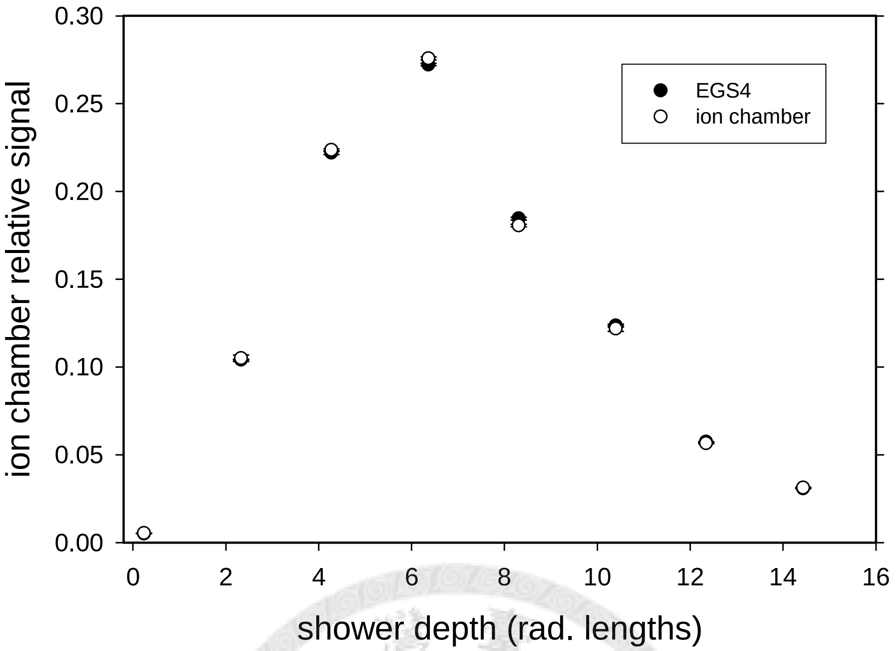

Figure 3.5: Ion chamber depth profile and EGS4 simulated depth profiles, both normalized so that the sum of points is unity.

alumina, the fluorescence chamber, and the ion chamber are included in the simulation modeling. The comparison between the ionization data and the EGS4 simulation results is shown in Fig. 3.5. The rations of simulation to observation at various depths are plotted in Fig. 3.6. The RMS deviation of the ratios is 1.9%, and the discrepancies are less than 4% at all depths. This is an adequate validation of the simulation of the longitudinal profile for the purposes of this work,.

For consideration of background signals from the penetrating neutrons, it is simulated using FLUKA [52]. This is folded with a value reported for the sensitivity of the helium to neutrons [53]. The signal fraction from neutrons in the worst case, 14 RL, is 9×10^{-4} and so can be neglected.

3.2.2 Transverse Shower Profile

For the transverse profiles measured by the screen-camera system, only data from the first shower event in each data run are used to avoid the effect of the long decay time. The

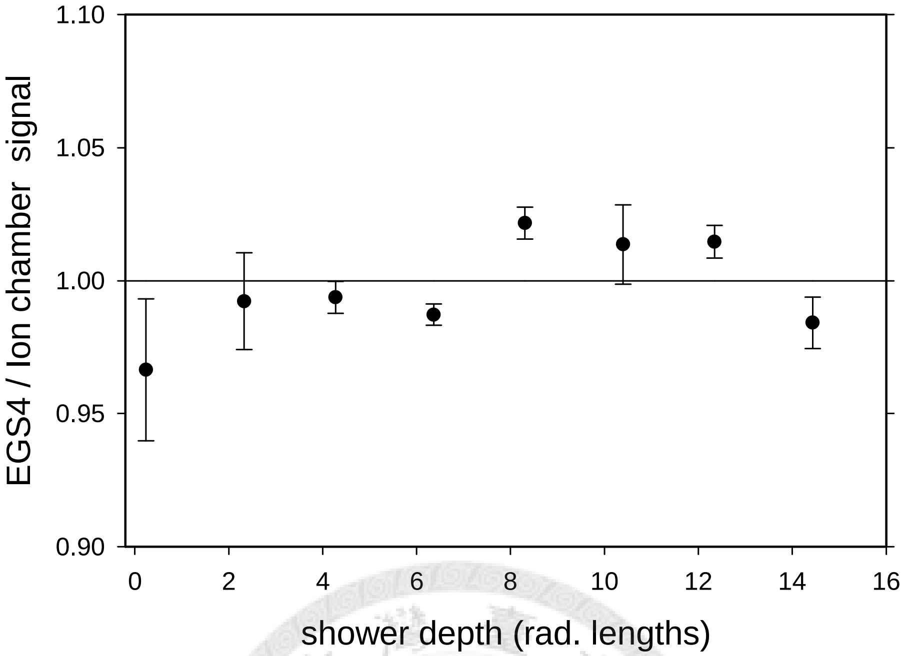

Figure 3.6: Ratios of EGS4 simulation results to ionization data at various shower depths, where the simulation and data depth profiles are both normalized to unity.

transverse spreads of the showers are exemplified by the 10 RL case, where the shower is widely spread but the signals remain strong (see Fig. 3.7). Signals from ± 4.8 cm vertical range are projected on to the horizontal axis. The profile measured by the scintillation screen and camera is compared with the results of the EGS4 simulation. The agreement in the transverse distribution is adequate for our purposes. The transverse containment of the showers by the fluorescence chamber and the ion chamber is evidently well modeled by the simulations. The characteristic sharp central peak can be seen even at 10 RL. It is this peak that causes the small nonlinear effect in the ion chamber measurement.

3.2.3 Longitudinal Shower Fluorescence Profile

The PMT signals are plotted against the toroid signals pulse by pulse. As an example, the signals from the PMT number 4 against the beam intensities measured by the toroid at 6 RL are plotted in Fig. 3.8. Data in the lower lobe are backgrounds taken with the shutter in place. The background levels in different runs are monitored using the two hooded

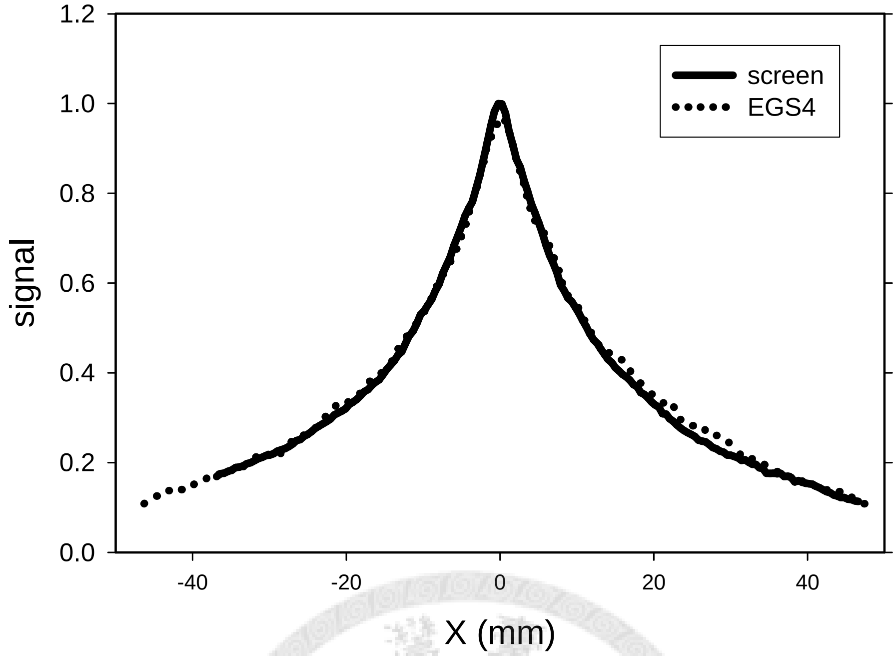

Figure 3.7: Shower spread at 10 radiation lengths. Signals from ± 4.8 cm y-axis range are projected on to x-axis.

PMT.

Straight line fits are applied to the data points. In order to address concerns of possible saturation in the PMT response, PMT pulse heights are restricted by limiting the beam intensities. The intensities used for each plot correspond to PMT average pulse heights that are expected to deviate from linearity by less than 2%. Various upper limits of the beam intensities are performed to check the sensitivity of the fits to this restriction. For limits varying by a factor of 2, the fitted slopes vary on average by less than ±1%, except for the very weak signal at near-zero shower depth, which vary by ±11%. These variations in slope are taken as systematic uncertainties and included in the overall uncertainties. The background slopes from the shutter-in runs are corrected by the background levels measured by the hooded PMT. The uncertainties from all slope fits are included in the final error estimates. The resulting fluorescence shower profiles from three PMT using the HiRes filter are shown in Fig. 3.9.

Simulation using EGS4 is also performed to simulate the energy deposit in the air

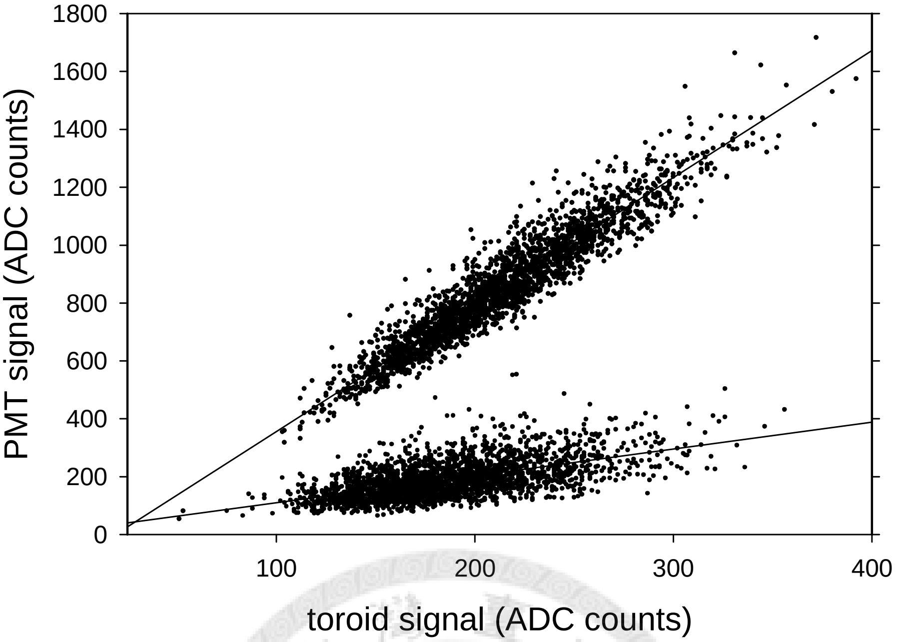

Figure 3.8: An example of the correlation between signals from PMT 4 and the beam toroid at 6 radiation lengths. Both signal and background data are shown.

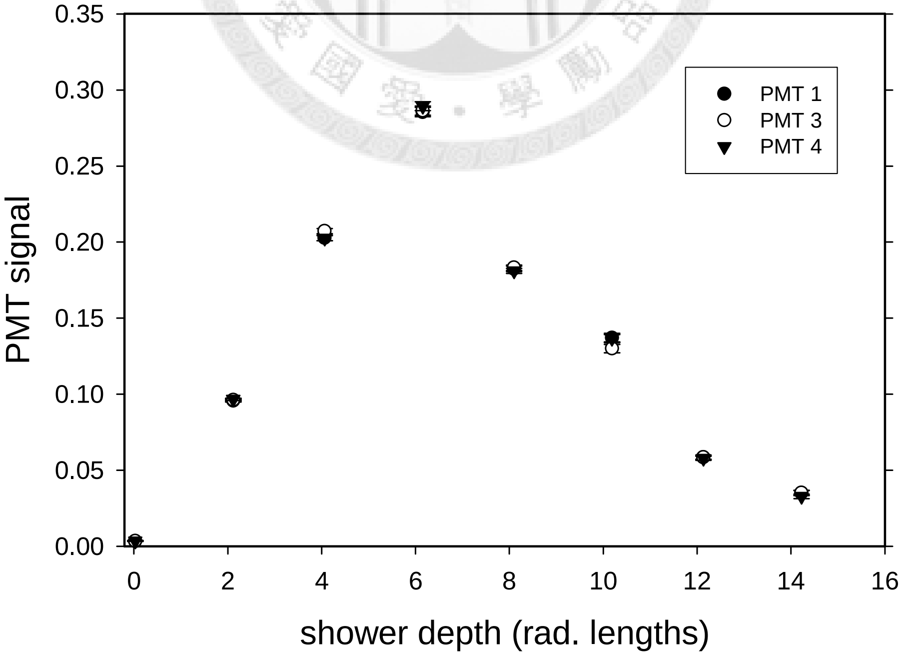

Figure 3.9: Shower fluorescence profiles for the three PMTs, each normalized so that the sum of its points is unity.

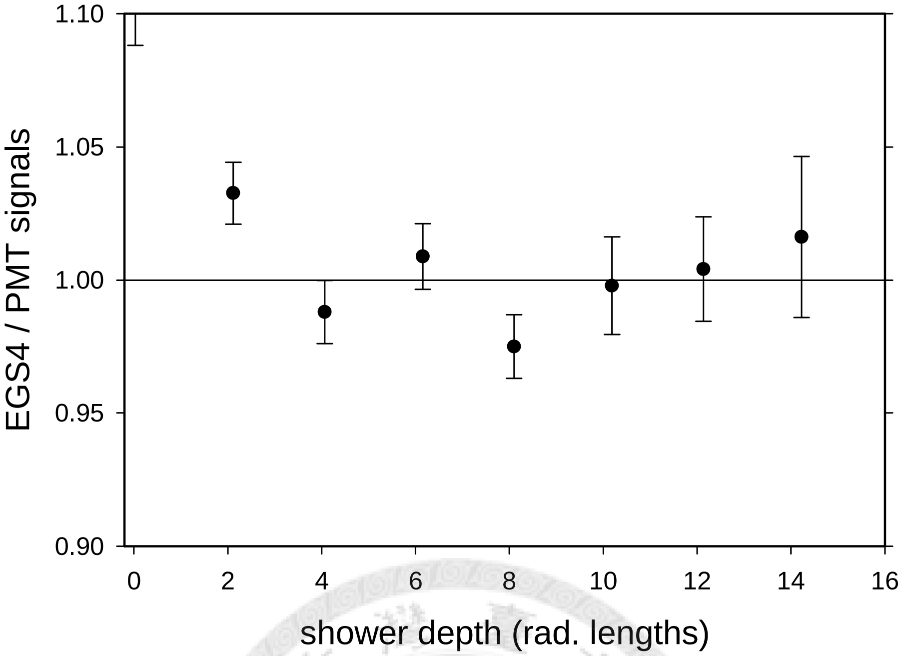

Figure 3.10: Ratio of EGS4 simulation results to weighted average of PMT signals vs. shower depth.

space in the fluorescence chamber. The energy deposit is weighted with factors to account for the volume shapes seen by the PMT, optical solid angles, and an approximation for the change in filter transmission with light incident angle. Acceptance differences between the tubes ware found to be small. The ratio of the energy deposit simulated by EGS4 to the weighted average of the PMT signals is shown in Fig. 3.10. The sum of the signals is normalized to unity for each profile. The fluorescence data agree with the simulations within less than 4%, except for the point at near-zero shower depth, where the very weak signals have large uncertainties. Excluding the point at minimal depth, the RMS deviation of the ratios is 1.9%. This is the accuracy that the fluorescence light yield is measured to follow the energy deposit simulations.

It is seen that the energy deposit simulations are validated by both comparisons with direct ionization measurement and with fluorescence measurement. The fluorescence and ionization longitudinal shower profiles are plotted together in Fig. 3.11. The ratios between the signals are not made since the material thicknesses are different in the two

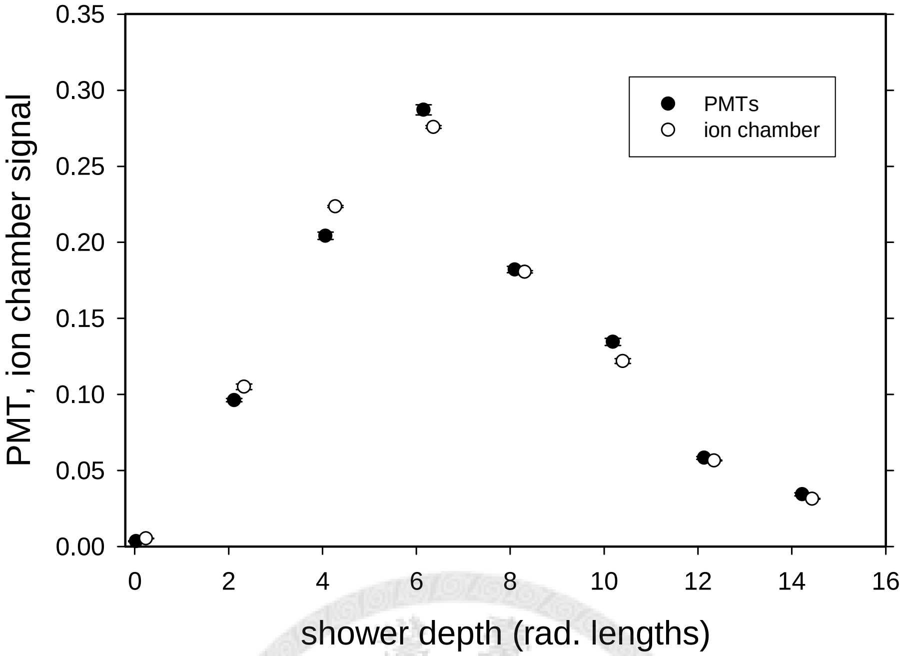

Figure 3.11: Comparison of fluorescence and ionization longitudinal profiles. The shower depths are slightly different between the two cases. The sums of their points are independently normalized to unity.

cases.

Some data are also taken with the bandpass optical filters. The ratios of bandpass signals to non-filter signal are shown in Fig. 3.12. It is seen that the emission spectrum is not altered significantly at different shower depths.

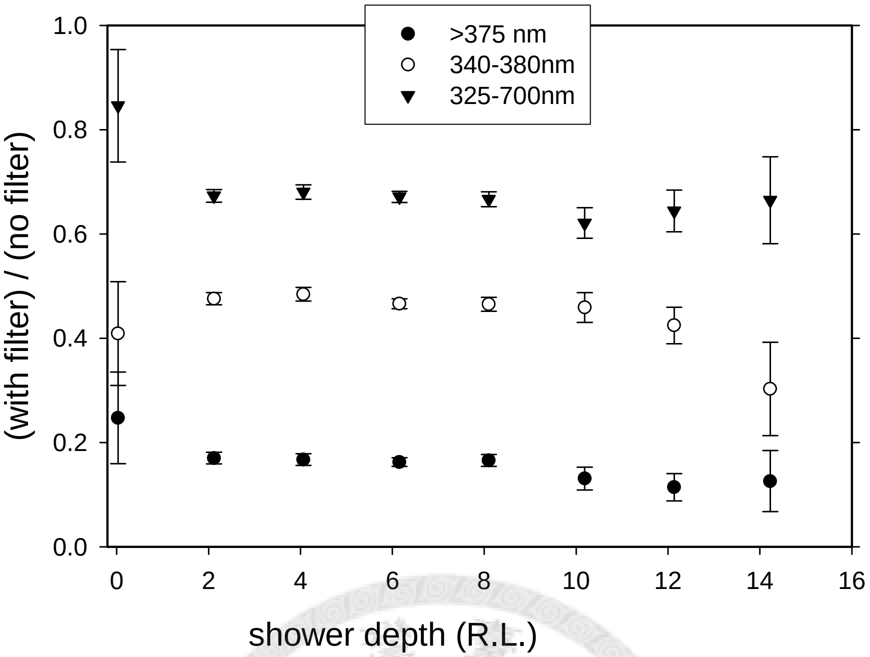

Figure 3.12: Comparison between bandpass and wide band optical filters at different shower depths. The emission spectrum is not altered significantly at different shower depths.

3.3 Conclusions

The results in this experiment validate the shower reconstruction technique used for the UHECR fluorescence detectors, that is, the fluorescence emission is proportional to the energy deposit in the shower development. The technique used in this experiment can be further developed to benchmark shower simulation codes at higher precision that may be needed for future UHECR detectors.

The overall FLASH experiment is a step to help toward precise UHECR measurements. It is a also a successful example to demonstrate the potential of laboratory astrophysics, which studies astro or astro-induced events via validated scaling, with controllable variables in the laboratory .

Part II

Constraining the Nature of Dark Energy

Chapter 4

Introduction

4.1 Dark Energy

Compelling evidences from Type Ia supernovae (SN Ia) and other cosmological observations show that the expansion of the universe is undergoing an accelerating stage at late times (see Ref. [54] for a review). Within the framework of general relativity and assuming homogeneity and isotropy, this indicates that there should exist an energy source, termed dark energy, which provides a significant negative pressure to cause this acceleration. Perhaps the simplest solution to this is achieved by adding a nonzero "cosmological constant" to the Einstein's equations. However, its value is expected by quantum field theory to be 10^{120} times larger than is observed, which is embarrassing.

Thus far the nature of dark energy remains unresolved and is generally regarded as one of the most tantalizing problems in cosmology. While a positive cosmological constant remains the simplest realization of dark energy, current observational data have not ruled out the possibility of a time-evolving dark energy [55]. In the pursuit of revealing the nature of dark energy, cosmological observations serve to constrain the behavior of dark energy. Theoretical studies, on the other hand, should determine whether dark energy models can be tested and distinguished by their observational consequences. As one awaits more information from the future observations, the constraining power of the next-generation observations and new analysis methods are being pursued (see Ref. [55]–[62] and Ref. [11, 12] for examples).

Many dark energy models have been proposed and studied. For the cosmological constant, its value has been constrained by observations (see Ref. [63] for example). The quintessence model, which invokes a time-varying scalar field [64]–[66], generally allows its energy density and equation of state to evolve with time. There are various quintessence models with different potential forms (see Ref. [67]–[70] and Ref. [58] for examples) that have been proposed. Studies of the classification [71, 72] and the general dynamical behavior [73] of quintessence have been carried out. There have been also works on the reconstruction of quintessence potentials (see Ref. [73]–[80] and Ref. [11]) and the investigations on how future observational data can constrain individual models of quintessence [56]–[58]. The generalized Chaplygin gas (see Ref. [81] and references therein) has been proposed to either unify dark matter and dark energy [82] or to simply play the role of dark energy [83, 84]. The constraint of the generalized Chaplygin gas has been obtained [84]–[86]. While these works have helped us study the possible nature of dark energy and obtain constraints of the parameters of an individual dark energy model, it should be desirable to explore possible means to determine whether a particular dark energy model can be ruled out by the observational data.

In this part of the thesis, we test dark energy models with a new approach and discriminate the models on the phase plane of dark energy equation of state, both based on current observational data.

4.2 Testing Dark Energy Models

We introduce a new approach to testing the consistency between a dark energy model and the observational data [11, 12]. For each dark energy model, we look for a *characteristic*, $Q(z)$, which in general can vary with the redshift but is equivalent to a constant parameter within the domain of the model. We further define the *measure of consistency*, $\mathcal{M}(z)$, as the derivative of $Q(z)$ with respect to the redshift z. The observational data should allow a null value for $\mathcal{M}(z)$ if the corresponding dark energy model is consistent with them. If, however, the $\mathcal{M}(z) = 0$ line lies outside certain confidence region, then that dark energy model is ruled out by the observational data at the corresponding confidence level. To obtain the constraint on the measure of consistency $\mathcal{M}(z)$ from the observational data, a parametrization of the relevant physical quantity, such as the equation of state or the luminosity distance, is required. We have invoked a broadly used form of parametrization of the equation of state [87, 88, 55],

$$w(z) = p_{\rm DE}(z)/\rho_{\rm DE}(z) = w_0 + w_a(1-a) = w_0 + w_a z/(1+z)\,, \tag{4.1}$$

where $p_{\rm DE}(z)$ and $\rho_{\rm DE}(z)$ are the pressure and the energy density of dark energy, respectively. The two parameters in Eq. (4.1) and the normalized matter density at present, Ω_m, define the parameter space, (w_0, w_a, Ω_m), through which the information from the observational data can be extracted. A recent work that is close in spirit to ours is that of Zunckel and Clarkson [62], who proposed consistency test of the cosmological constant via a direct parametrization of the luminosity distance. In our terminology, they use $Q(z) = 1 - \rho_{\rm DE}(z)/\rho_c$, which is equivalent to the constant Ω_m in the domain of the cosmological constant, where ρ_c is the critical density at present. Sahni et al. [61] also proposed null test of the cosmological constant via the diagnostic $Om(z) = (H^2(z)/H_0^2 - 1)/[(1+z)^3 - 1]$, which is equivalent to the constant Ω_m in the domain of the cosmological constant, where $H(z)$ is the Hubble expansion rate and H_0 is the Hubble constant.

We take the current data set and apply our method of consistency test to five dark energy models, including the cosmological constant, the generalized Chaplygin gas as the dark energy component [83, 84], and three quintessence models: exponential, power-law and inverse-exponential potentials [69, 70]. The data set we use includes a recently compiled "Constitution set" of SN Ia data [89]–[95], the cosmic microwave background (CMB) measurement from the five-year Wilkinson Microwave Anisotropy Probe (WMAP) observation [63], and the baryon acoustic oscillation (BAO) measurement from the Sloan Digital Sky Survey (SDSS) [96] and the 2dF Galaxy Redshift Survey (2dFGRS) [97].

A conventional way to determine how well a dark energy model can fit the observational data is the *model-based approach*, in which one optimizes the parameters of each dark energy model based on the observational data and then statistically assesses the goodness of fit (see Ref. [86], for example). In such approach one has to obtain the best fit for each set of parameters specific to the particular dark energy model, which could be tedious. In particular, in order to optimize the parameters of a quintessence model one has to solve the field equation numerically for each point in the parameter space, which can be computationally intensive and time consuming [57]. In contrast, in our approach we first constrain the parameters of the chosen parametrization through the observational data, and then test consistency of each dark energy model based on this set of parameters. This can be more efficient than the model-based approach when one deals with a large number of dark energy models. It is also more direct and therefore much faster to constrain the parameter space (w_0, w_a, Ω_m) than to optimize the parameters of a quintessence model in the model-based approach. The potential downside of our method, however, would be that as long as one invokes a specific form of parametrization, one might have simultaneously imposed a prior, or bias, against certain dark energy models. This issue requires a separate investigation and we are currently pursuing that [98]. We note that the two methods are different in spirit. The goodness of fit describes how well a model can fit the observations. The consistency test, on the other hand, examines whether the condition necessary for a model is excluded by the observations. With in mind the pros and cons mentioned above, we believe that the two methods, that is, the model-based and ours, should be complimentary to each other in the pursuit of revealing the nature of dark energy.

4.3 Discriminating Dark Energy Models

The ratio of pressure to energy density for dark energy, the equation of state $w = p/\rho$, is the characteristic of how the energy density evolves with time. The cosmological constant relates to the constant equation of state $w = -1$, while other dark energy models generally have time-evolving w. The time-derivative of w in units of the Hubble time, $w' = dw/dlna$, characterizes the dynamical behavior of the equation of state. Studies of the dynamical behaviors and classification of dark energy models in the w–w' phase plane have been carried out [71, 72, 100, 101, 102]. It is found that different dark energy models are bounded in different sectors in the w–w' plane.

On the one hand, we gather the bounds for various dark energy models in the w–w' plane. On the other hand, we obtain the constraints on the w–w' plane in the redshift region $0 < z < 1$, by adopting a widely used parametrization [87, 88, 55], $w(z) = w_0 + w_a(1-a) = w_0 + w_a z/(1+z)$, based on the current observational data. We then compare the dark energy models with the constraints on the w–w' plane for $0 < z < 1$ [13]. The work close to ours is that of Barger et al. [103], in which they used the old data set and examined the dark energy models only at the redshift $z = 1$ in the w_0–w_a plane.

Chapter 5

Consistency Test of Dark Energy Models[*]

5.1 Consistency test of dark energy models

We perform consistency test of five dark energy models including the cosmological constant, the exponential potential, the power-law potential, the inverse-exponential potential, and the generalized Chaplygin gas as the dark energy component.

For each dark energy model, we look for a *characteristic*, $Q(z)$, which in general can vary with the redshift but is equivalent to a constant parameter within the domain of the model. We further define the *measure of consistency*, $\mathcal{M}(z)$, as the derivative of $Q(z)$ with respect to the redshift z. The observational data should allow a null value for $\mathcal{M}(z)$ if the corresponding dark energy model is consistent with them. If, however, the $\mathcal{M}(z) = 0$ line lies outside certain confidence region, then that dark energy model is ruled out by the observational data at the corresponding confidence level.

5.1.1 Formalism

We consider a flat Friedmann-Lemaitre-Robertson-Walker (FLRW) universe and assume that it is dominated by pressureless matter and dark energy in the present epoch. The

---

[*] The work has been published in New J. Phys. and Mod. Phys. Lett. A.[11, 12]

Hubble expansion rate, $H \equiv \dot{a}/a$, is given by the Friedmann equations as

$$\begin{aligned} H^2(z) &= \frac{8\pi G_N}{3}\left[\rho_m(z) + \rho_{\rm DE}(z)\right] \\ &= H_0^2\left[\Omega_m(1+z)^3 + (1-\Omega_m)\exp\left(3\int_0^z \left[1+w(z')\right]\frac{dz'}{1+z'}\right)\right], \end{aligned} \tag{5.1}$$

where the dark energy density

$$\rho_{\rm DE}(z) = \rho_c(1-\Omega_m)\exp\left(3\int_0^z \left[1+w(z')\right]\frac{dz'}{1+z'}\right), \tag{5.2}$$

and

$$\rho_c \equiv \frac{3H_0^2}{8\pi G_N}\,. \tag{5.3}$$

For quintessence as a dark energy model, the quintessence field and the potential are related to the equation of state, the Hubble expansion rate, and the dark energy density as follows [99, 11].

$$\phi(z) - \phi_0 = \pm\int_0^z \frac{\sqrt{\left[1+w(z')\right]\rho_{\rm DE}(z')}}{H(z')}\frac{dz'}{1+z'}, \tag{5.4}$$

$$V(z) = \left[1-w(z)\right]\rho_{\rm DE}(z)/2\,. \tag{5.5}$$

For the cosmological constant, the energy density ρ_Λ is a constant. We define the characteristic $Q_\Lambda(z)$ as the dark energy density $\rho_{\rm DE}(z)$, which in general would evolve with the redshift but is equivalent to the constant parameter ρ_Λ within the cosmological constant domain,

$$Q_\Lambda(z) \equiv \rho_{\rm DE}(z) \tag{5.6}$$

$$= \rho_\Lambda \quad \text{for the cosmological constant.} \tag{5.7}$$

In the same spirit, for the exponential potential,

$$V_{\rm exp}(\phi) = V_1\exp\left[-\phi/M_1\right], \tag{5.8}$$

we identify M_1 as the characteristic constant parameter and accordingly define the characteristic $Q_{\text{exp}}(z)$,

$$\begin{aligned} Q_{\text{exp}}(z) &\equiv -V(z)\left(\frac{dV}{d\phi}\right)^{-1}(z) && (5.9) \\ &= M_1 \quad \text{for the exponential potential.} && (5.10) \end{aligned}$$

For the power-law potential,

$$V_{\text{power}}(\phi) = m^{4-n}\phi^n\,, \tag{5.11}$$

we define the following characteristic corresponding to the index n,

$$\begin{aligned} Q_{\text{power}}(z) &\equiv \left[1 - V(z)\left(\frac{dV}{d\phi}(z)\right)^{-2}\frac{d^2V}{d\phi^2}(z)\right]^{-1} && (5.12) \\ &= n \quad \text{for the power-law potential.} && (5.13) \end{aligned}$$

For the inverse-exponential potential,

$$V_{\text{inverse-exp}}(\phi) = V_2 \exp\left[M_2/\phi\right]\,, \tag{5.14}$$

the characteristic is defined as

$$\begin{aligned} Q_{\text{inverse-exp}}(z) &\equiv -\frac{4}{V(z)}\left(\frac{dV}{d\phi}(z)\right)^3\left[\frac{d^2V}{d\phi^2}(z) - \frac{1}{V(z)}\left(\frac{dV}{d\phi}(z)\right)^2\right]^{-2} && (5.15) \\ &= M_2 \quad \text{for the inverse-exponential potential.} && (5.16) \end{aligned}$$

As the dark energy component, the generalized Chaplygin gas has an equation of state govern by

$$p_{\text{DE}}(z) = -A/\left[\rho_{\text{DE}}(z)\right]^{\alpha}\,, \tag{5.17}$$

where $\alpha \neq -1$ and $A > 0$. The corresponding characteristic is defined as

$$\begin{aligned} Q_{\text{Chaplygin}}(z) &\equiv -\frac{\rho_{\text{DE}}(z)}{w(z)}\frac{dw}{dz}(z)\left(\frac{d\rho_{\text{DE}}}{dz}(z)\right)^{-1} - 1 && (5.18) \\ &= \alpha \quad \text{for the generalized Chaplygin gas.} && (5.19) \end{aligned}$$

We then define the measure of consistency $\mathcal{M}_i(z)$ as the derivative of the characteristic $Q_i(z)$ with respect to the redshift for each dark energy model,

$$\begin{aligned} \mathcal{M}_i(z) &\equiv \frac{dQ_i}{dz}(z) && (5.20) \\ &= 0 \quad \text{for the corresponding dark energy model,} && (5.21) \end{aligned}$$

where i denotes "Λ", "exp", "power", "inverse–exp" and "Chaplygin", respectively. $\mathcal{M}_i(z)$ can in general evolve with the redshift but should be constant zero in the domain of the corresponding dark energy model.

5.1.2 Observational data and constraint

We use the combined data set from three types of observations including the SN Ia observation, the CMB measurement, and the BAO measurement.

We use the Constitution set of SN Ia data compiled by Hicken et al. (see Ref. [95] and Ref. [89]– [94]) which provides the information of the luminosity distance and the redshift. The luminosity distance-redshift relation is given by

$$d_L(z) = (1+z)\int_0^z \frac{dz'}{H(z')}. \tag{5.22}$$

We use the CMB shift parameter measured by the five-year WMAP observation [63],

$$R = \sqrt{\Omega_m H_0^2}\int_0^{1090.04} \frac{dz}{H(z)} = 1.710 \pm 0.019. \tag{5.23}$$

We use the BAO measurement from the joint analysis of the SDSS and 2dFGRS data [97, 96], which gives

$$D_V(0.35)/D_V(0.2) = 1.812 \pm 0.060, \tag{5.24}$$

where

$$D_V(z_{\text{BAO}}) = \left[(1+z_{\text{BAO}})^2 D_A^2(z_{\text{BAO}})\frac{z_{\text{BAO}}}{H(z_{\text{BAO}})}\right]^{1/3}, \tag{5.25}$$

and $D_A(z)$ is the angular diameter distance,

$$D_A(z) = \frac{1}{1+z}\int_0^z \frac{dz'}{H(z')}. \tag{5.26}$$

The constraint of the parameter space (w_0, w_a, Ω_m) is obtained by fitting the three parameters to this combined data set. The best fit of the parameters are found to be

$$w_0 = -0.89^{+0.12}_{-0.14}, \quad w_a = -0.18^{+0.71}_{-0.74}, \quad \Omega_m = 0.25^{+0.03}_{-0.02}.$$

The confidence regions of (w_0, w_a, Ω_m) is shown in Fig. 5.1.

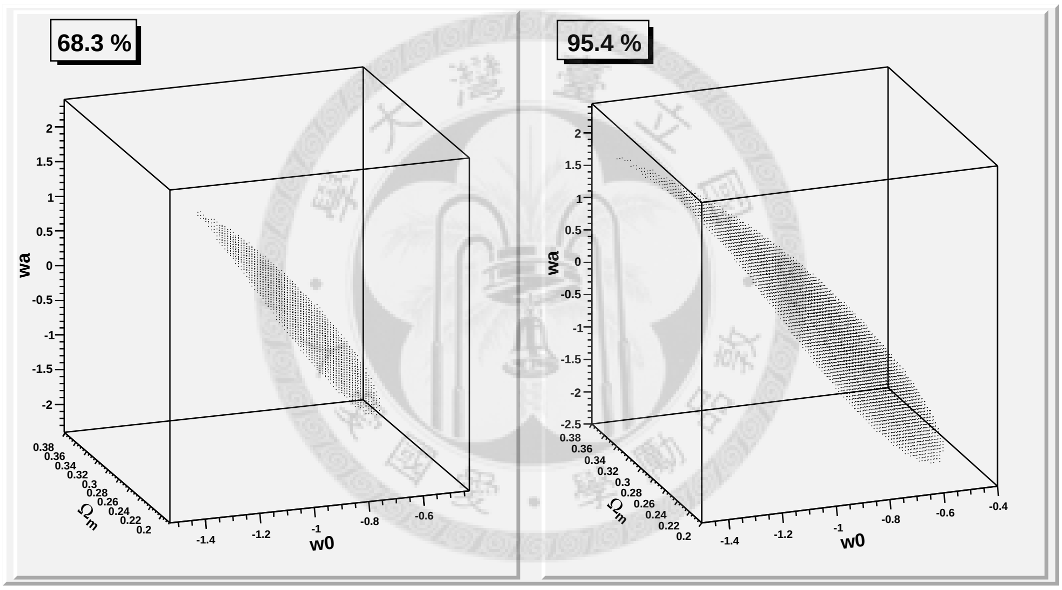

Figure 5.1: The joint three-dimensional constraint of (w_0, w_a, Ω_m) based on a combined data set including the Constitution set of SN Ia data, the CMB measurement from the five-year WMAP, and the BAO measurement from the SDSS and 2dFGRS. The left and the right figures correspond to the 68.3% and the 95.4% confidence regions, respectively.

5.1.3 Results of the consistency test

For the consistency test of each dark energy model, we reconstruct $\mathcal{M}_i(z)$ via the constraint of (w_0, w_a, Ω_m), with the use of the equations in Sec. 4.2 and Sec. 5.1.1. We perform the test in the redshift region $0 < z < 1.55$, where the influence of dark energy on the expansion of the universe is most significant. This region is covered by the current SN Ia observations, which is the most sensitive type of observations to probe the behavior of dark energy. If the $\mathcal{M}_i(z) = 0$ line lies outside certain confidence region, the corresponding dark energy model is ruled out at that confidence level. Adopting the constraint obtained in Sec. 5.1.2, we find that the $\mathcal{M}_{\text{exp}}(z) = 0$ line lies outside the 95.4% confidence region while the null lines of the other four models lie inside the 68.3% confidence region. The results are shown in Fig. 5.2.

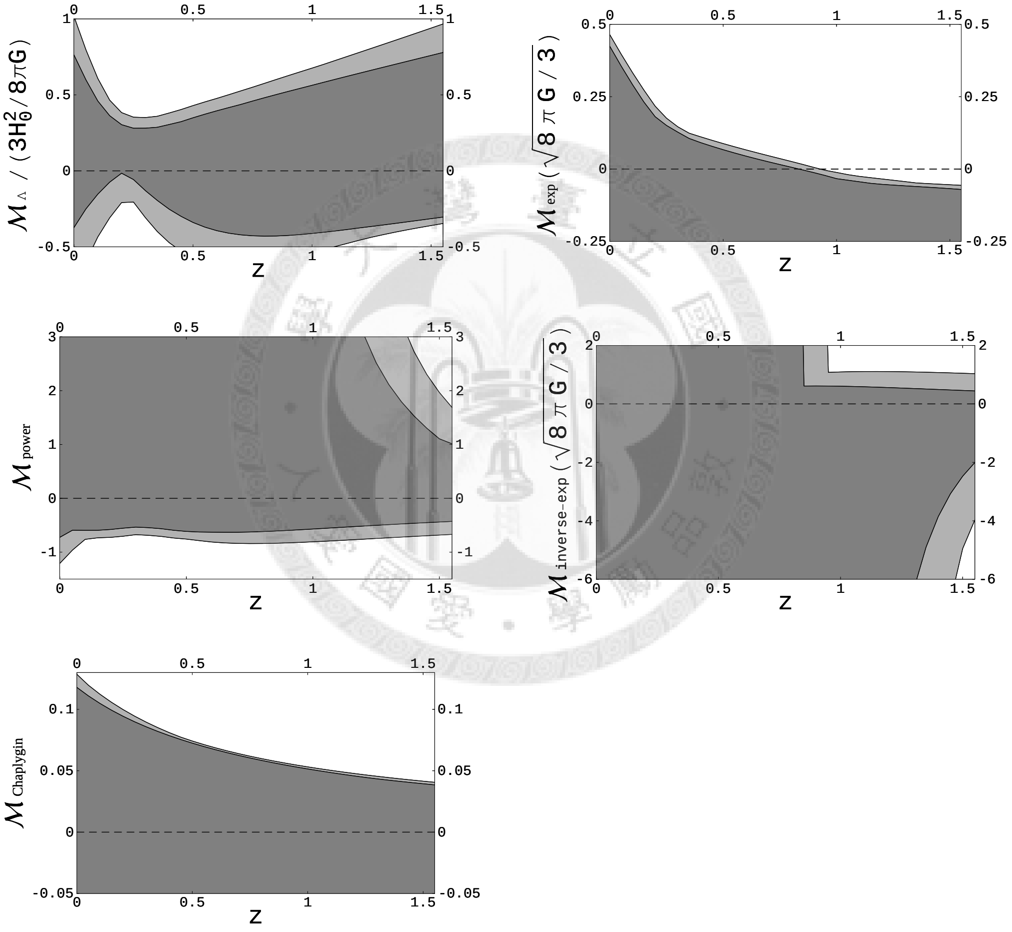

Figure 5.2: The measure of consistency of the five dark energy models. The dark and light gray areas correspond to the 68.3% and 95.4% confidence regions, respectively. The $\mathcal{M}_{\text{exp}}(z) = 0$ line lies outside the 95.4% confidence region for $0.95 < z < 1.55$. The null lines of the measure for the other four models lie inside the 68.3% confidence regions for $0 < z < 1.55$. This indicates that the exponential potential is ruled out at the 95.4% confidence level while the other four dark energy models are still consistent with the current observational constraints down to the 68.3% confidence level.

5.2 Summary

We have preformed consistency test of five dark energy models, including the cosmological constant, the generalized Chaplyngin gas, and three quintessence models: exponential, power-law, and inverse-exponential potentials. This test gives a simple signature if a dark energy model is ruled out by the observational data. It can be done efficiently via the constraint of a single set of parameters deduced from the observational data, and can test quintessence models without solving the field equation.

Through our approach and invoking the broadly used parametrization of the equation of state, the exponential potential is found to be ruled out at the 95.4% confidence level based on the current observational data. The other four dark energy models remain consistent with the current observations down to the 68.3% confidence level. It is worth noticing that in our previous work the power-law potential was ruled out at the 68.3% confidence level based on a different data set [11]. One noticeable change in the new data set is that the cosmological constant is contained in the 68.3% confidence region, which was not so in the previous one. Whether our method can discriminate between the power-law potential and the cosmological constant can in principle be studied with the Monte Carlo test [98]. The flat cosmological constant model was examined by Davis et al. [86] via the model-based approach using a different data set. They found the goodness of fit for the flat cosmological constant model to be 43.7% while we find the model at least consistent with the data at the 68.3% confidence level. The two results are not in conflict with each other.

This method of consistency test can in principle be applied not only to other dark energy models but also to other models explaining the accelerating expansion, as long as one can identify a characteristic $Q(z)$ that corresponds to a constant parameter of each model. One can also choose a different parametrization for better discriminating power between the models in regard. The discriminating power of the method with different forms of parametrization and the possible bias imposed by the chosen parametrization should be studied via the Monte Carlo test [98].

Chapter 6

Constraints on the Phase Plane of the Dark Energy Equation of State[*]

6.1 Classification of dark energy models

Quintessence

The quintessence model [64]–[66], which invokes a time-varying scalar field, generally allows its energy density and equation of state to evolve with time, and has $w > -1$. The equation of motion of the quintessence field is $\ddot{\phi} + 3H\dot{\phi} + V_{,\phi} = 0$, where $H = \dot{a}/a$ is the Hubble expansion rate, and $V_{,\phi} = dV/d\phi$. In terms of w and w', the equation of motion can be written as [70]

$$\mp\frac{V_{,\phi}}{V} = \sqrt{\frac{3(1+w)}{\Omega_\phi(a)}}\left[1 + \frac{1}{6}\frac{d\ln(x_q)}{d\ln(a)}\right], \tag{6.1}$$

where the minus sign corresponds to $\dot{\phi} > 0$ and the plus sign to the opposite, $\Omega_\phi(a)$ is the dimensionless energy density of the quintessence field, and $x_q = (1+w)/(1-w)$. For the down-rolling quintessence field ($\dot{V} < 0$), the left-hand side of Eq. (6.1) is positive, and the bound of w and w' can be obtained as $w' > -3(1-w)(1+w)$ [100, 101]. The up-rolling quintessence field ($\dot{V} > 0$) takes the other side, $w' < -3(1-w)(1+w)$. The bound of the tracker quintessence [69] is obtained in [100, 101]. However, strong acceleration

---

[*] This work has been submitted to Phys. Lett. B.[13]

today, with $w \lesssim -0.7$, requires the breakdown of tracking [72]. The bound should only apply to the high redshift [72], $z \gg 1$, which is not the region of interest in this paper. A conjectured limit of quintessence has been proposed in [72] as $V/(-V_{,\phi}) < M_P$, where M_P is the Plank mass. However, the physical origin of this limit is not clear [72]. We therefore do not impose this constraint on the quintessence model. Caldwell and Linder identified two categories of quintessence models, "thawing" and "freezing", based on their dynamical behavior [71]. For the thawing models, the equation of state is $w \approx -1$ at early times, but grows less negative with time as $w' > 0$. The bounds of the thawing models are $(1+w) < w' < 3(1+w)$. For the freezing models, initially the equation of state is $w > -1$ with $w' < 0$, but the field is frozen at late times where $w \to -1$ and $w' \to 0$. The bounds of the freezing models are $3w(1+w) < w' < 0.2w(1+w)$. Note that the upper bound for the freezing models is only valid for $z < 1$.

Phantom

The phantom model has negative kinetic energy and the equation of state $w < -1$ [104]. The equation of motion of the phantom field is $\ddot{\phi} + 3H\dot{\phi} - V_{,\phi} = 0$. In terms of w and w', the equation of motion can be written as [105]

$$\pm\frac{V_{,\phi}}{V} = \sqrt{\frac{-3(1+w)}{\Omega_\phi(a)}}\left[1 + \frac{1}{6}\frac{d\ln(x_p)}{d\ln(a)}\right], \tag{6.2}$$

where the plus sign corresponds to $\dot{\phi} > 0$ and the minus sign to the opposite, $\Omega_\phi(a)$ is the dimensionless energy density of the phantom field, and $x_p = -(1+w)/(1-w)$. For the up-rolling phantom field ($\dot{V} > 0$), the left-hand side of Eq. (6.2) is positive, and the bound of w and w' can be obtained as $w' < -3(1-w)(1+w)$. The down-rolling phantom field ($\dot{V} < 0$) takes the other side $w' > -3(1-w)(1+w)$. Note that Eq. (6.2) and the bounds are different from those obtained in [101].

Barotropic fluids

Barotropic fluids are those for which the pressure is an explicit function of the energy density, $p = f(\rho)$ (see [102] and references therein). The expression for w' can be written as [100, 102]

$$w' = -3(1+w)\left(\frac{dp}{d\rho} - w\right). \tag{6.3}$$

The sound speed for a barotropic fluid is given by $c_s^2 = dp/d\rho$. To ensure stability, we must have $c_s^2 \geq 0$, which gives the bound $w' \leq 3w(1+w)$ for non-phantom ($w > -1$) barotropic fluids [100, 102]. For causality, we further require $c_s^2 \leq 1$ [106], which gives the bound $w' \geq -3(1+w)(1-w)$ for $w > -1$ [102].

The classification of the above-mentioned dark energy models in the w–w' plane is shown in Fig. 6.1. Note that all of the bounds are valid at late times for $0 < z < 1$.

6.2 Constraints on the w–w' plane

6.2.1 Observational data

We use the combined data set described in Sec. 5.1.2. We assume that the universe is flat in this work.

To obtain the constraints on the w–w' plane, we invoke a broadly used form of parametrization of the equation of state [87, 88, 55],

$$w(z) = w_0 + w_a(1-a) = w_0 + w_a z/(1+z)\,. \tag{6.4}$$

The constraint of w_0, w_a and Ω_m is obtained by fitting the three parameters to this combined data set. The estimate of the parameters are found to be $w_0 = -0.89^{+0.12}_{-0.14}, \quad w_a = -0.18^{+0.71}_{-0.74}, \quad \Omega_m = 0.25^{+0.03}_{-0.02}$. The two-dimensional constraint of w_0–w_a is obtained and shown in Fig. 6.2.

6.2.2 Results of the constraints on the w–w' plane

We reconstruct the constraints on the w–w' plane via the two-dimensional constraint of w_0–w_a, with the use of Eq. (6.4) and $w'(z) = -aw_a = -w_a/(1+z)$, at late times for $0 < z < 1$. The cosmological constant is outside the 68.3% confidence region for all redshifts. We also find that the phantom models, the up-rolling quintessence models, and

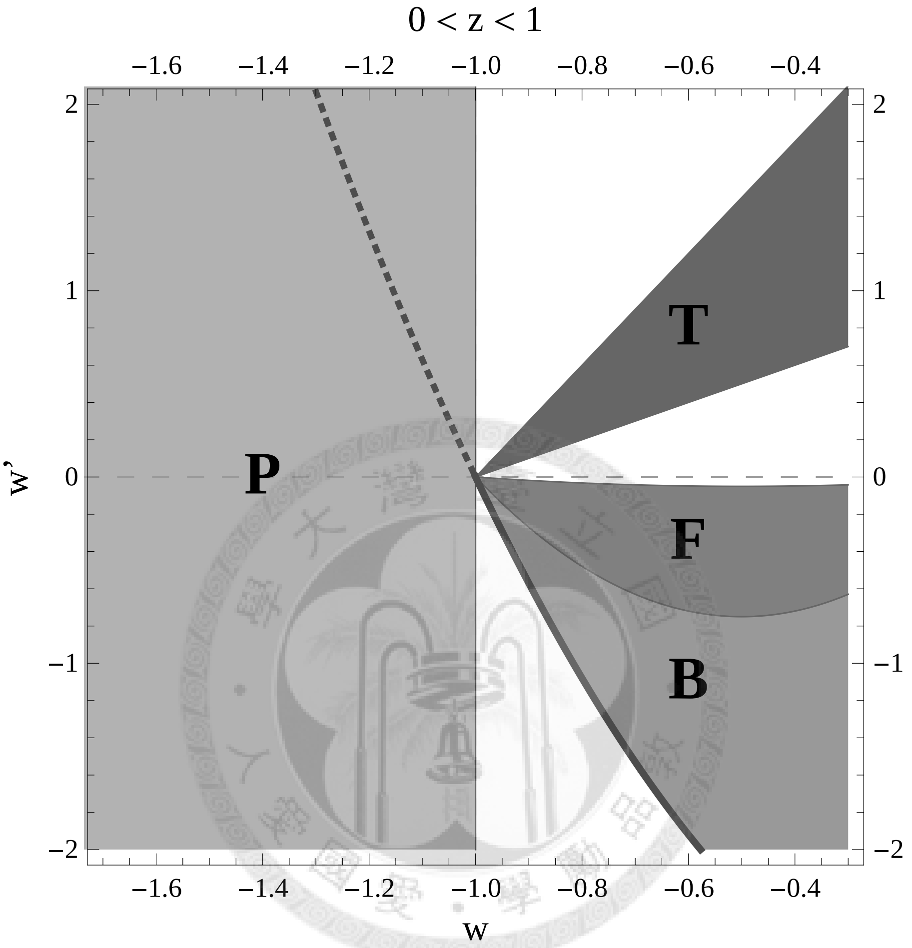

Figure 6.1: Classification of dark energy models in the w–w' plane. Models are separated by the solid curves. The symbols “T”, “F”, “B”, and “P” denote the “thawing”, “freezing”, “non-phantom barotropic”, and “phantom” models, respectively. The quintessence models correspond to the region for $w > -1$. The cosmological constant corresponds to the point $(-1, 0)$. The bold solid curve is both the lower bound for the non-phantom barotropic models and the bound that separates the down-rolling and up-rolling quintessence models (down-rolling takes the upper side). The dotted curve is the bound that separates the down-rolling and up-rolling phantom models (up-rolling takes the lower side).

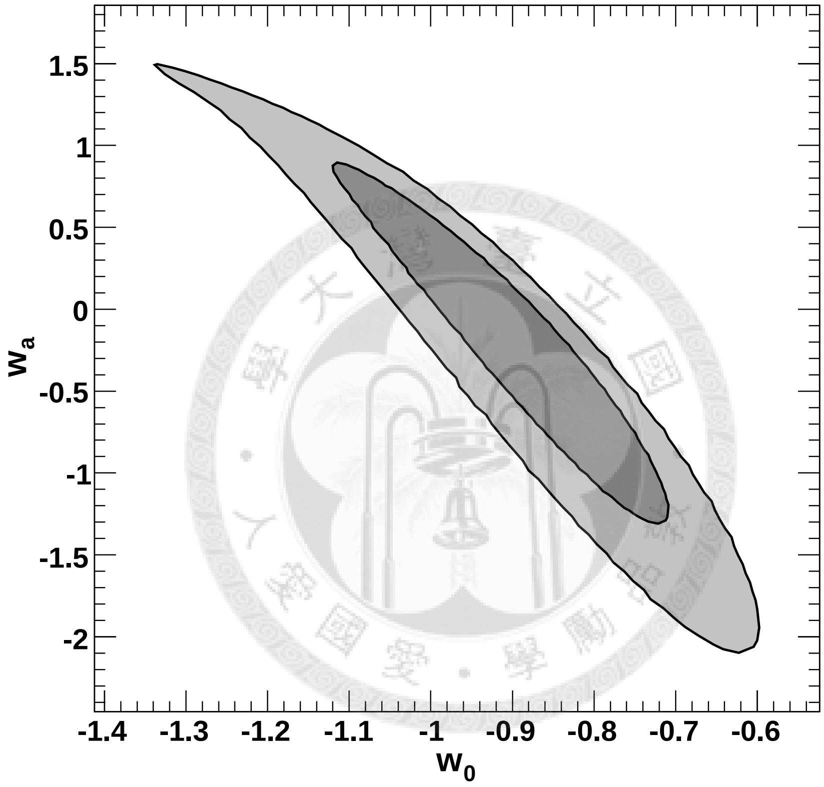

Figure 6.2: The two-dimensional constraint of w_0–w_a based on the combined data set including the Constitution set of SN Ia data, the CMB measurement from the five-year WMAP, and the BAO measurement from the SDSS and 2dFGRS. The dark and the light gray areas correspond to the 68.3% and the 95.4% confidence regions, respectively.

the non-phantom barotropic fluids lie outside the 68.3% confidence region in the redshift regions $0.18 < z < 0.22$, $0.4 < z < 1$ and $0.7 < z < 1$, respectively. The down-rolling quintessence models overlap with the 68.3% confidence region for $0 < z < 1$. Those include the thawing and the freezing models. All of the models in regards overlap with the 95.4% confidence region for $0 < z < 1$. Samples of the constraints on the w–w' plane at redshifts $z = 0$, $z = 0.2$ and $z = 1$, together with models are shown in Fig. 6.3.

6.3 Conclusion and discussion

Applying the bounds for various dark energy models in the w–w' plane for redshift $0 < z < 1$, we find that models including the cosmological constant, phantom, non-phantom barotropic fluids, and up-rolling quintessence are ruled out at the 68.3% confidence level based on the current observational data. Down-rolling quintessence, including the thawing and the freezing models, is consistent with the current observations. All the models in regards are still consistent with the data at the 95.4% confidence level. Using the same SN Ia data set, Shafieloo et al. [107] also found the data inconsistent with the cosmological constant at the 68.3% confidence level if the assumption of a constant equation of state is dropped. Barger et al. [103] found the non-phantom barotropic fluids excluded at the 95.4% confidence level based on the old data set. We notice that there was a time the observations favored $w(z = 0) \leq -1$ [91] but now the observations favor $w(z = 0) \geq -1$. However, the conclusions are drawn at the 68.3% confidence level at most. It is hoped that the next-generation observations will constraint the dark energy equation of state an order of magnitude better [54, 55]. We shall be able to identify dark energy at higher confidence in the coming future.

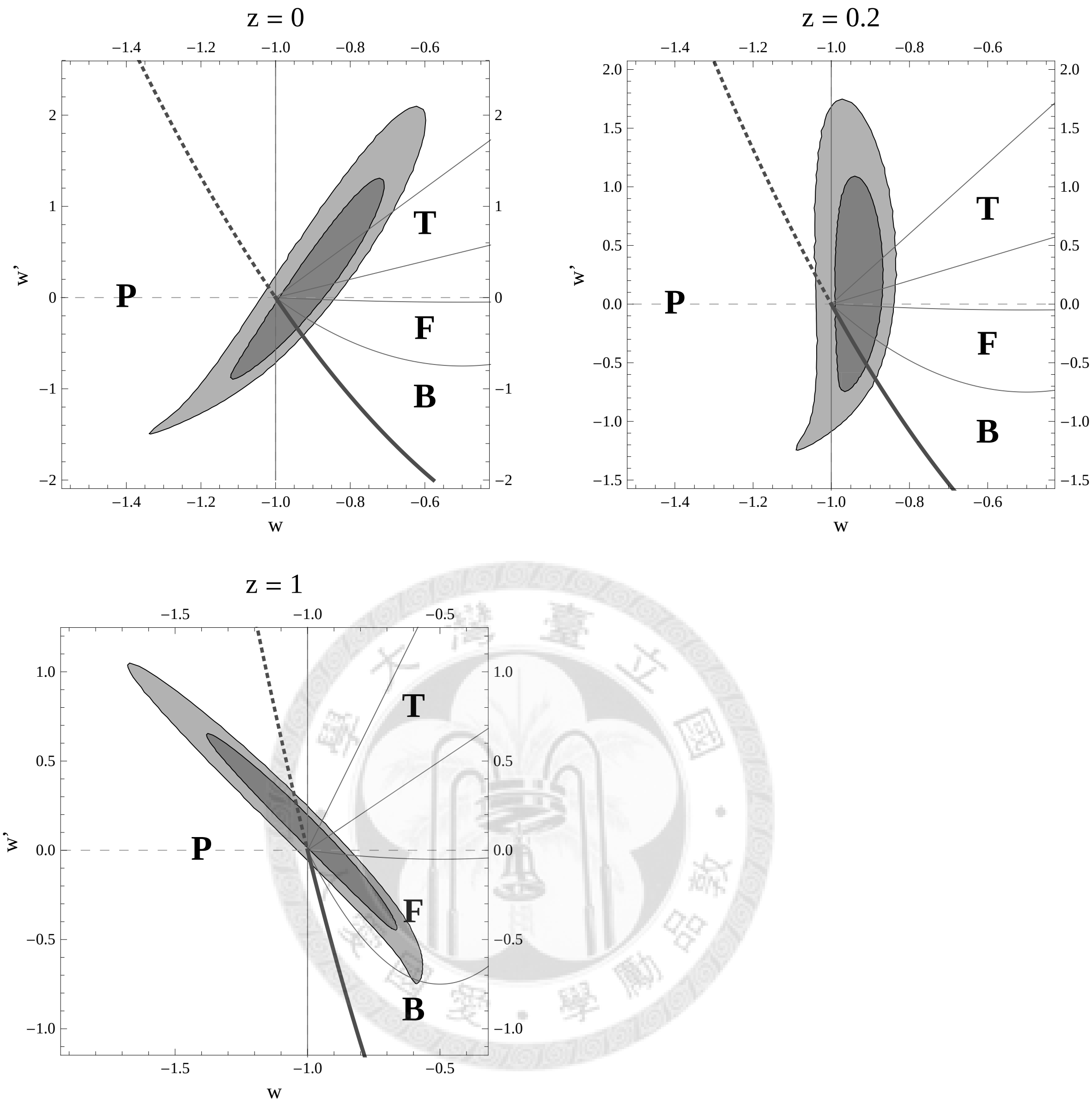

Figure 6.3: Samples of the constraints on the w–w' plane at redshifts $z = 0$, $z = 0.2$ and $z = 1$. The dark and the light gray areas correspond to the 68.3% and the 95.4% confidence regions, respectively. See the caption in Fig. 6.1 for the description of the regions to that the models belong. The cosmological constant is outside the 68.3% confidence region for all redshifts. The down-rolling phantom models lie outside the 68.3% confidence region at $z = 0$ and $z = 0.2$. All the phantom models lie outside the 68.3% confidence region at $z = 0.2$. Both the up-rolling quintessence models and the non-phantom barotropic fluids lie outside the 68.3% confidence region at $z = 1$. The down-rolling quintessence models including the thawing and the freezing models overlap with the 68.3% confidence region at all of the three redshift. All of the models in regards overlap with the 95.4% confidence region at all of the three redshifts.

Bibliography

[1] V. F. Hess, Phys. Zeitschr. 13 (1912) 1084.

[2] J. Linsley, Phys. Rev. Lett. 10, 146 (1963).

[3] E. Hubble, Proceedings of the National Academy of Sciences of the United States of America, Volume 15, Issue 3, pp. 168-173 (1929).

[4] A. A. Penzias and R. W. Wilson, Astrophys. J. vol. 142, p.419-421 (1965).

[5] A. G. Riess *et al.* [Supernova Search Team Collaboration], Astron. J. **116**, 1009 (1998) [arXiv:astro-ph/9805201].

[6] S. Perlmutter *et al.* [Supernova Cosmology Project Collaboration], Astrophys. J. **517**, 565 (1999) [arXiv:astro-ph/9812133].

[7] J. Belz *et al.*, Astropart. Phys. **25**, 57 (2006) [arXiv:astro-ph/0510375].

[8] R. Abbasi *et al.*, Astropart. Phys. **29**, 77 (2008) [arXiv:0708.3116 [astro-ph]].

[9] R. Abbasi *et al.* [FLASH Collaboration], Nucl. Instrum. Meth. A **597**, 32 (2008).

[10] R. Abbasi *et al.* [FLASH Collaboration], Nucl. Instrum. Meth. A **597**, 37 (2008).

[11] Je-An Gu, C.-W. Chen and P. Chen, New J. Phys. 11 (2009) 073029 [arXiv:0803.4504 [astro-ph]].

[12] C.-W. Chen, Je-An. Gu and P. Chen, Mod. Phys. Lett. A. Vol. 24, No. 21 (2009) pp. 1649-1657 [arXiv:0903.2423 [astro-ph.CO]].

[13] C.-W. Chen, P. Chen and Je-An Gu, arXiv:0905.2738 [astro-ph.CO], submitted to Phys. Lett. B.

[14] M. Nagano and A. A. Watson, Rev. Mod. Phys. **72**, 689 (2000).

[15] J. Bluemer, R. Engel and J. R. Hoerandel, arXiv:0904.0725 [astro-ph.HE].

[16] E. Waxman, Phys. Rev. Lett. 75 (1995) 386; M. Vietri, Astrophys. J. 453 (1995) 883; T.K. Gaiser, F. Halzen and T. Stanev, Phys. Rep. 258 (1995) 173; K. Mannheim, Astropart. Phys. 3 (1995) 295.

[17] M. Birkel and S. Sarkar, Astropart. Phys 9, (1998) 297; P. Battacharjee, C.T. Hill and D.N. Schramm Phys. Rev. Lett. 69, (1992) 567; R.J. Protheroe and T. Stanev, Phys. Rev. Lett. 77 (1996) 3708; M. Birkel and S. Sarkar, Astropart. Phys. 9 (1998) 297; P. Battacharjee and G. Sigl, Phys. Rep. 327 (2000) 109.

[18] K. Greisen, Phys. Rev. Letters 16 (1966) 748; V.A. Kuzmin, G.T. Zatsepin, Pisma Zh. Eksp. Teor. Fiz. 4 (1966) 114, JETP Letters 4, 78.

[19] M. Takeda et al., Astrophys. J. 522 (1999) 225.

[20] R. Abbasi *et al.* [HiRes Collaboration], Phys. Rev. Lett. **100**, 101101 (2008) [arXiv:astro-ph/0703099].

[21] J. Abraham *et al.* [Pierre Auger Collaboration], Phys. Rev. Lett. **101**, 061101 (2008) [arXiv:0806.4302 [astro-ph]].

[22] A. Chiavassa *et al.* (KASCADE Collab.), Proc. of 29th Int. Cosmic Ray Conf., Pune 6 (2005) 313. M. Kestel *et al.*, Nucl. Instrum. Meth. A 535 (2004) 139; H. Klages *et al.* (Pierre Auger Collab.), Proc. of 30th Int. Cosmic Ray Conf., Merida 5 (2007) 849; M. C. Medina *et al.*; Nucl. Instrum. Meth. A566 (2006) 302–311; C. C. H. Jui (TA Collab.), Proc. of 29th Int. Cosmic Ray Conf., Pune 8 (2005) 327; D. Nitz *et al.* (Pierre Auger Collab.), Proc of 30th Int. Cosmic Ray Conf., Merida 5 (2007) 889; Y. Takahashi *et al.* (EUSO Collab.), Proc. of 30th Int. Cosmic Ray Conf., Merida 5 (2007) 1145.

[23] For a summary and references, see Particle Data Group, Phys. Letters B592 (2004), 242.

[24] A.N. Bunner, Ph.D. Thesis, Cornell University (1967).

[25] F. Blanco and F. Arqueros, Phys Letters A 345 (2005) 355.

[26] B. Keilhauer et al., Astropart. Phys. 25 (2006) 259.

[27] F. Arqueros et al., Astropart. Phys. 26 (2006) 231.

[28] G. Davidson and R. O'Neil, Jour. Chem. Phys 41 (1964) 3946.

[29] M. Nagano et al., Astropart. Phys. 20 (2003) 293.

[30] M. Nagano et al., Astropart. Phys. 22 (2004) 235.

[31] F. Kakimoto et al., Nucl. Instr. Meth. A 372 (1996) 527.

[32] J. Belz et al., Astropart. Phys., 25 (2006) 129.

[33] P. Colin et al., Astropart. Phys. 27 (2007) 317.

[34] M. Ave et al., arXiv:astro-ph/0703132v1, submitted to Elsevier Science.

[35] G. Lefeuvre et al., Nucl. Instr. Meth. A 578 (2007) 78.

[36] Reports of work in progress by various groups, made to the 4th Air Fluorescence Workshop, Prague, 2006, may be found at http.//www.particle.cz/conferences/floret2006/index.html.

[37] Qimaging scientific camera, http://www.qimaging.com/index.php

[38] Robert H. Simmons and Johnny S. T. Ng, Nucl. Instr. Meth. A 575 (2007) 334.

[39] Photonis, Brive La Gaillard, France, www.photonis.com.

[40] Spectra-Physics, Stratford, CT 06616, USA, model 77400.

[41] Hamamatsu Photonics K.K., Shizuoka-ken 438-0193, Japan; model H-7260-03.

[42] Newport Corp., Mountain View, CA; model VSL337ND-S

[43] LaserProbe Inc., Utica, NY 13502; model RjP-734.

[44] A. Bucholtz, Appl. Opt. 34 (1995) 2765.

[45] B. Bodhaine et al., Oceanic Technol., 16 (1999) 1854.

[46] Hamamatsu Photonics K.K., Shizuoka-ken 438-0193, Japan; model S2281.

[47] W.R. Nelson, H. Hiragama and D.W.O. Rogers, ”The EGS4 Code System", SLAC-265, Stanford Linear Accelerator Center (1985).

[48] J.S.T. Ng et al., Phys. Rev. Letters 87 (2001) 244801-1.

[49] Edmund Optics, Barrington, NJ08007 U.S.A., www.edmundoptics.com.

[50] Nova Phase Inc., Newton, NJ07860, U.S.A., www.novaphase.com.

[51] CERN Applications Software Group, Geneva, Switzerland (1993).

[52] A. Fasso et al., Proc Monte Carlo 2000 Conference, Lisbon 2000, Springer Verlag, Berlin (2001) 159, 955; A. Fasso et al., Proc. Conference for Computing in High Energy and Nuclear Physics (CHEP 2003), La Jolla, California, e-Print Archive physics/0306162.

[53] D. Indurthy et al., Nucl. Instr. Meth. A 258 (2004) 731.

[54] J. Frieman, M. Turner and D. Huterer, *Ann. Rev. Astron. Astrophys.* **46**, 385 (2008) [arXiv:0803.0982 [astro-ph]].

[55] A. Albrecht *et al.*, arXiv:astro-ph/0609591.

[56] M. Barnard, A. Abrahamse, A. Albrecht, B. Bozek and M. Yashar, *Phys. Rev.* D **77**, 103502 (2008) [arXiv:0712.2875 [astro-ph]].

[57] A. Abrahamse, A. Albrecht, M. Barnard and B. Bozek, *Phys. Rev.* D **77**, 103503 (2008) [arXiv:0712.2879 [astro-ph]].

[58] B. Bozek, A. Abrahamse, A. Albrecht and M. Barnard, *Phys. Rev.* D **77**, 103504 (2008) [arXiv:0712.2884 [astro-ph]].

[59] M. Barnard, A. Abrahamse, A. J. Albrecht, B. Bozek and M. Yashar, *Phys. Rev.* D **78**, 043528 (2008) [arXiv:0804.0413 [astro-ph]].

[60] Y. Wang and P. Mukherjee, *Phys. Rev.* D **76**, 103533 (2007) [arXiv:astro-ph/0703780].

[61] V. Sahni, A. Shafieloo and A. A. Starobinsky, *Phys. Rev.* D **78**, 103502 (2008) [arXiv:0807.3548 [astro-ph]].

[62] C. Zunckel and C. Clarkson, *Phys. Rev. Lett.* **101**, 181301 (2008) [arXiv:0807.4304 [astro-ph]].

[63] E. Komatsu *et al.* [WMAP Collaboration], *Astrophys. J. Suppl.* **180**, 330 (2009) [arXiv:0803.0547 [astro-ph]].

[64] R. R. Caldwell, R. Dave and P. J. Steinhardt, *Phys. Rev. Lett.* **80**, 1582 (1998) [arXiv:astro-ph/9708069].

[65] Je-An Gu and W-Y. P. Hwang, *Phys. Lett.* B **517**, 1 (2001) [arXiv:astro-ph/0105099].

[66] L. A. Boyle, R. R. Caldwell and M. Kamionkowski, *Phys. Lett.* B **545**, 17 (2002) [arXiv:astro-ph/0105318].

[67] J. A. Frieman, C. T. Hill, A. Stebbins and I. Waga, *Phys. Rev. Lett.* **75**, 2077 (1995) [arXiv:astro-ph/9505060].

[68] A. J. Albrecht, C. P. Burgess, F. Ravndal and C. Skordis, *Phys. Rev.* D **65**, 123507 (2002) [arXiv:astro-ph/0107573].

[69] I. Zlatev, L. Wang and P. J. Steinhardt, *Phys. Rev. Lett.* **82**, 896 (1999) [arXiv:astro-ph/9807002];

[70] P. J. Steinhardt, L. Wang and I. Zlatev, *Phys. Rev.* D **59**, 123504 (1999) [arXiv:astro-ph/9812313].

[71] R. R. Caldwell and E. V. Linder, *Phys. Rev. Lett.* **95**, 141301 (2005) [arXiv:astro-ph/0505494].

[72] E. V. Linder, *Phys. Rev.* D **73**, 063010 (2006) [arXiv:astro-ph/0601052].

[73] D. Huterer and H. V. Peiris, *Phys. Rev.* D **75**, 083503 (2007) [arXiv:astro-ph/0610427].

[74] D. Huterer and M. S. Turner, *Phys. Rev.* D **60**, 081301 (1999) [arXiv:astro-ph/9808133].

[75] A. A. Starobinsky, *JETP Lett.* **68**, 757 (1998) [*Pisma Zh. Eksp. Teor. Fiz.* **68**, 721 (1998)] [arXiv:astro-ph/9810431].

[76] T. Nakamura and T. Chiba, *Mon. Not. Roy. Astron. Soc.* **306**, 696 (1999) [arXiv:astro-ph/9810447].

[77] T. D. Saini, S. Raychaudhury, V. Sahni and A. A. Starobinsky, *Phys. Rev. Lett.* **85**, 1162 (2000) [arXiv:astro-ph/9910231].

[78] B. F. Gerke and G. Efstathiou, *Mon. Not. Roy. Astron. Soc.* **335**, 33 (2002) [arXiv:astro-ph/0201336].

[79] V. Sahni and A. Starobinsky, *Int. J. Mod. Phys.* D **15**, 2105 (2006) [arXiv:astro-ph/0610026].

[80] M. Sahlen, A. R. Liddle and D. Parkinson, *Phys. Rev.* D **75**, 023502 (2007) [arXiv:astro-ph/0610812].

[81] M. C. Bento, O. Bertolami and A. A. Sen, *Phys. Rev.* D **66**, 043507 (2002) [arXiv:gr-qc/0202064].

[82] N. Bilic, G. B. Tupper and R. D. Viollier, *Phys. Lett.* B **535**, 17 (2002) [arXiv:astro-ph/0111325].

[83] A. Y. Kamenshchik, U. Moschella and V. Pasquier, *Phys. Lett.* B **511**, 265 (2001) [arXiv:gr-qc/0103004].

[84] A. A. Sen and R. J. Scherrer, *Phys. Rev.* D **72**, 063511 (2005) [arXiv:astro-ph/0507717].

[85] M. Makler, S. Quinet de Oliveira and I. Waga, *Phys. Lett.* B **555**, 1 (2003) [arXiv:astro-ph/0209486].

[86] T. M. Davis *et al.*, *Astrophys. J.* **666**, 716 (2007) [arXiv:astro-ph/0701510].

[87] M. Chevallier and D. Polarski, *Int. J. Mod. Phys.* D **10**, 213 (2001) [arXiv:gr-qc/0009008].

[88] E. V. Linder, *Phys. Rev. Lett.* **90**, 091301 (2003) [arXiv:astro-ph/0208512].

[89] A. G. Riess *et al.* [Supernova Search Team Collaboration], *Astrophys. J.* **607**, 665 (2004) [arXiv:astro-ph/0402512].

[90] P. Astier *et al.* [The SNLS Collaboration], *Astron. Astrophys.* **447**, 31 (2006) [arXiv:astro-ph/0510447].

[91] A. G. Riess *et al.*, *Astrophys. J.* **659**, 98 (2007) [arXiv:astro-ph/0611572].

[92] G. Miknaitis *et al.*, *Astrophys. J.* **666**, 674 (2007) [arXiv:astro-ph/0701043].

[93] W. M. Wood-Vasey *et al.* [ESSENCE Collaboration], *Astrophys. J.* **666**, 694 (2007) [arXiv:astro-ph/0701041].

[94] M. Kowalski *et al.*, *Astrophys. J.* **686**, 749 (2008) [arXiv:0804.4142 [astro-ph]].

[95] M. Hicken *et al.*, arXiv:0901.4804 [astro-ph.CO].

[96] D. J. Eisenstein *et al.* [SDSS Collaboration], *Astrophys. J.* **633**, 560 (2005) [arXiv:astro-ph/0501171].

[97] W. J. Percival, S. Cole, D. J. Eisenstein, R. C. Nichol, J. A. Peacock, A. C. Pope and A. S. Szalay, *Mon. Not. Roy. Astron. Soc.* **381**, 1053 (2007) [arXiv:0705.3323 [astro-ph]].

[98] C.-W. Chen, Je-An Gu and P. Chen (in preparation).

[99] Z. K. Guo, N. Ohta and Y. Z. Zhang, *Phys. Rev.* D **72**, 023504 (2005) [arXiv:astro-ph/0505253].

[100] R. J. Scherrer, Phys. Rev. D 73, 043502 (2006) [arXiv:astro-ph/0509890].

[101] T. Chiba, Phys. Rev. D 73, 063501 (2006) [arXiv:astro-ph/0510598].

[102] E. V. Linder and R. J. Scherrer, arXiv:0811.2797 [astro-ph].

[103] V. Barger, E. Guarnaccia and D. Marfatia, Phys. Lett. B 635, 61 (2006) [arXiv:hep-ph/0512320].

[104] R. R. Caldwell, Phys. Lett. B 545, 23 (2002) [arXiv:astro-ph/9908168].

[105] J. Kujat, R. J. Scherrer and A. A. Sen, Phys. Rev. D 74, 083501 (2006) [arXiv:astro-ph/0606735].

[106] G. Ellis, R. Maartens and M. A. H. MacCallum, Gen. Rel. Grav. 39, 1651 (2007) [arXiv:gr-qc/0703121].

[107] A. Shafieloo, V. Sahni and A. A. Starobinsky, arXiv:0903.5141 [astro-ph.CO].